Comparison between $\mu^-\mu^+$ and e^-e^+ colliders for charged Higgs production in the 2HDM

Brahim Ait Ouazghour,[1,*] Abdesslam Arhrib,[2,3,†] Kingman Cheung,[3,4,‡] Es-said Ghourmin,[5,§] and Larbi Rahili[5,‖]

[1]*LPHEA, Physics Department, FSSM, Cadi Ayyad University, P.O.B. 2390 Marrakech, Morocco*
[2]*Abdelmalek Essaadi University, FST Tanger B.P. 416, Morocco*
[3]*Department of Physics and CTC, National Tsing Hua University, Hsinchu, Taiwan 300*
[4]*Division of Quantum Phases and Devices, School of Physics, Konkuk University, Seoul 143-701, Republic of Korea*
[5]*Laboratory of Theoretical and High Energy Physics (LPTHE), Faculty of Science, Ibnou Zohr University, B.P. 8106, Agadir, Morocco*

(Received 4 September 2023; accepted 6 May 2024; published 11 June 2024)

We study the phenomenology of the charged Higgs boson at future muon colliders. We investigate the pair production $\mu^+\mu^- \to H^+H^-$, the single production $\mu^+\mu^- \to W^\pm H^\mp$, as well as the vector boson fusion (VBF) $\{e^+e^-, \mu^+\mu^-\} \to \nu\bar{\nu}H^+H^-$. We show that the neutral Higgs exchange diagrams in the muon collider case can lead to a significant boost in the cross sections through their Yukawa couplings. Our results for the muon collider are systematically compared to the corresponding ones at e^+e^- machines. It is demonstrated that the VBF $e^+e^- \to \nu\bar{\nu}H^+H^-$ can compete with the mentioned $2 \to 2$ processes. We select benchmark points and perform signal-background analyses, taking into account detector simulations. We demonstrate the discovery region at 5σ and the excluded region at 2σ levels at a 3 TeV muon collider.

DOI: 10.1103/PhysRevD.109.115009

I. INTRODUCTION

The Standard Model (SM) spectrum was completed with the discovery of a scalar particle that exhibits properties similar to those of the SM Higgs boson by ATLAS [1] and CMS [2] in 2012. The majority of measurements regarding the Higgs couplings and cross sections conducted at the LHC are in good agreement with the theoretical framework of the SM [3,4]. So, with the new LHC run and its projected high luminosity option [5], we are now entering an era of precise measurement programs at the LHC to scrutinize the SM.

Despite its success in explaining various phenomena and its predictions aligning with experimental results, however, the SM still exhibits weaknesses, including challenges related to dark matter and dark energy, matter-antimatter asymmetry, the hierarchy problem, and neutrino mass generation. These weaknesses suggest that the SM is merely a low-energy effective theory of a more fundamental one that is yet to be discovered. Several beyond-the-SM (BSM) theories near the TeV scale [6–10] naturally incorporate an extended Higgs sector.

Among the many extensions of BSM theories, the two-Higgs-doublet model (2HDM) is notable for its simplicity, positioning it as a candidate for a BSM model. It can address certain limitations of the Standard Model, such as providing a mechanism for CP violation and explaining the matter-antimatter asymmetry in the Universe. The 2HDM is also featured in several high-energy (UV) theories motivated by naturalness and dark matter considerations, like the minimal supersymmetric Standard Model (MSSM). In view of this, an additional $SU(2)_L$ Higgs doublet is added and the Higgs spectrum is indeed widened compared to the Standard Model (SM). This results in a total of five physical Higgs particles [11], including a pair of singly charged Higgs bosons ($H^\pm$); the latter can be abundantly produced at both hadron and e^+e^- colliders.

At hadron colliders, the charged Higgs boson can be produced through several channels: from the top decay when the charged-Higgs mass is less than $m_t - m_b$, associated production with a top quark through gluon-gluon fusion or gluon-bottom quark annihilation, and a number of other processes (for a review see Ref. [12]). Meanwhile, at e^+e^- colliders, the dicharged Higgs boson is mainly produced through the s-channel process $e^+e^- \to \gamma^*, Z^* \to H^+H^-$ [13]. Consequently, its rate depends solely

*b.ouazghour@gmail.com
†aarhrib@gmail.com
‡cheung@phys.nthu.edu.tw
§s.ghourmin123@gmail.com
‖rahililarbi@gmail.com

on the charged Higgs boson mass and gauge couplings [14,15]. The contribution from s-channel diagrams involving neutral Higgs exchange is proportional to the electron mass (m_e) and is thus significantly suppressed. Similarly, the associate production $e^+e^- \to W^\pm H^\mp$ in the 2HDM [16,17] and in the MSSM [18–20] is only mediated at the one-loop level, with the tree-level cross section being suppressed by m_e^2 [16–20]. Finally, associated pairwise production of dicharged Higgs boson with $\nu_e\bar{\nu}_e$ is still possible at e^+e^- colliders, and depends on the gauge couplings of the charged Higgs as we will see further on in this study.

Therefore, the discovery of nonstandard Higgs bosons at colliders, most notably at the LHC (see Ref. [21]), would validate one or more models beyond the SM (BSM). The absence of such a discovery so far has led to current bounds on the masses and couplings of the non-SM Higgs bosons. The high luminosity LHC (HL-LHC) will improve some of the aforementioned measurements and may find hints of the presence of new physics. However, to pursue such a precise measurement program that was initiated at the LHC, there is a consensus or need to build a clean environment electron-positron Higgs factory [22–24], which allows detailed studies of the novel SM-like Higgs boson. Several projects for e^+e^- machines are planned, including the Circular Electron Positron Collider (CEPC) [25], the Compact Linear Collider (CLIC) [26,27], the Future Circular Collider (FCC-ee) [28,29], and the International Linear Collider (ILC) [30–32].

The muon collider (MuC) concept has been around since the 1960s. However, there has been renewed interest in muon colliders operating at high energies in the range of multi-TeV [33–35] in recent years. There exist a number of studies that suggested the possibility of using the muon collider to detect electroweak dark matter [36] and to discover heavy particles from BSM physics [37–39]. The primary reasons for building a muon collider are that it offers significant physics opportunities to open an unprecedented new energy frontier for new physics and to provide a clean leptonic-collision environment for precision studies [36,37,40–46].

Charged-Higgs pair production and its associated production with a W gauge boson at the future muon collider have been studied in the context of the minimal supersymmetric Standard Model (MSSM) [47,48] and of the 2HDM with CP violation [49]. In this work, we investigate charged Higgs boson production at the future muon collider in the framework of the 2HDM with different Yukawa textures, by investigating the following $2 \to 2$ processes: $\mu^+\mu^- \to H^\pm H^\mp$ and $\mu^+\mu^- \to W^\pm H^\mp$. Both processes have additional contributions from the s-channel neutral-Higgs exchange and the t-channel neutrino exchange due to the large Yukawa of the muon. These new contributions may enhance/suppress the cross section at the muon collider with respect to the e^+e^- case, given the fact that the muon mass is about 207 times larger than the electron mass. Furthermore, the presence of neutral-Higgs exchange in the s channel for both processes may offer the possibility of resonance enhancement. Additionally, the process $\mu^+\mu^- \to W^\pm H^\mp$ offers the possibility of searching for the charged Higgs with mass up to $\sqrt{s} - m_W$, in contrast to $\mu^+\mu^- \to H^\pm H^\mp$, which only probes up to $m_{H^\pm} < \sqrt{s}/2$. We will also show that the vector boson fusion (VBF) $e^+e^- \to \nu\bar{\nu}H^+H^-$ can compete with the aforementioned $2 \to 2$ processes.

We present results for different Yukawa textures of the 2HDM. The 2HDM types II and X are of particular interest, as the neutral-Higgs coupling to a pair of muons experiences enhancement in the large $\tan\beta$ limit and may increase the cross section accordingly. Our numerical results are presented after scrutinizing the 2HDM parameter space by imposing various theoretical constraints (unitarity, perturbativity, and vacuum stability) and experimental ones [from SM-like Higgs boson discovery data, BSM Higgs boson exclusions data, electroweak precision tests (EWPT) and flavor physics]. In the allowed parameter space, we then calculate the signal and various SM backgrounds, followed by a full Monte Carlo (MC) analysis and estimations of the sensitivity at the center-of-mass energy $\sqrt{s} = 3$ TeV.

The paper is structured as follows: we begin with a brief review of the 2HDM in the following section, discussing the scalar sector, the various couplings required, and the relevant theoretical and experimental constraints. Then, we present the details of the calculations for $\mu^+\mu^- \to H^\pm H^\mp$ and $\mu^+\mu^- \to W^\pm H^\mp$ in Sec. III. Section IV presents the numerical results of our study taking into account theoretical constraints, flavor-physics constraints, as well as experimental ones from LEP-II, Tevatron, and LHC. In Sec. V, we detail the Monte Carlo analysis and calculate the significance for the charged-Higgs discovery at the 3 TeV muon collider. Lastly, we provide our concluding remarks in Sec. VI.

II. 2HDM REVIEW, THEORETICAL AND EXPERIMENTAL CONSTRAINTS

A. 2HDM review

We briefly discuss the basic features of the two-Higgs-doublet model (2HDM) [11,50] and the various Yukawa textures [51,52]. In the 2HDM, in addition to SM doublet Φ_1, a new doublet Φ_2 with a hypercharge $+1$ is added to the Higgs sector, where we assume that CP is not spontaneously broken. The two Higgs-scalar doublets can be parametrized by

$$\Phi_1 = \begin{pmatrix} \phi_1^+ \\ \phi_1^0 \end{pmatrix} \quad \text{and} \quad \Phi_2 = \begin{pmatrix} \phi_2^+ \\ \phi_2^0 \end{pmatrix} \tag{1}$$

with $\phi_i^0 = (v_i + \psi_i + i\eta_i)/\sqrt{2}$, $i = 1, 2$. The general scalar potential $SU(2)_L \times U(1)_Y$ invariant under the SM transformations can be written as [11]

TABLE I. Yukawa couplings of the h, H, and A Higgs bosons to the quarks and leptons in the 2HDM.

	κ_h^u	κ_h^d	κ_h^l	κ_H^u	κ_H^d	κ_H^l	κ_A^u	κ_A^d	κ_A^l
Type-I	c_α/s_β	c_α/s_β	c_α/s_β	s_α/s_β	s_α/s_β	s_α/s_β	c_β/s_β	$-c_\beta/s_\beta$	$-1/\tan\beta$
Type-II	c_α/s_β	$-s_\alpha/c_\beta$	$-s_\alpha/c_\beta$	s_α/s_β	c_α/c_β	c_α/c_β	c_β/s_β	s_β/c_β	$\tan\beta$
Type-X	c_α/s_β	c_α/s_β	$-s_\alpha/c_\beta$	s_α/s_β	s_α/s_β	c_α/c_β	c_β/s_β	$-c_\beta/s_\beta$	$\tan\beta$
Type-Y	c_α/s_β	$-s_\alpha/c_\beta$	c_α/s_β	s_α/s_β	c_α/c_β	s_α/s_β	c_β/s_β	s_β/c_β	$-1/\tan\beta$

$$V(\Phi_1,\Phi_2) = m_{11}^2\Phi_1^\dagger\Phi_1 + m_{22}^2\Phi_2^\dagger\Phi_2 - [m_{12}^2\Phi_1^\dagger\Phi_2 + \text{H.c.}] + \frac{\lambda_1}{2}(\Phi_1^\dagger\Phi_1)^2 + \frac{\lambda_2}{2}(\Phi_2^\dagger\Phi_2)^2 + \lambda_3(\Phi_1^\dagger\Phi_1)(\Phi_2^\dagger\Phi_2) + \lambda_4(\Phi_1^\dagger\Phi_2)(\Phi_2^\dagger\Phi_1) + \left\{\frac{\lambda_5}{2}(\Phi_1^\dagger\Phi_2)^2 + \text{H.c.}\right\}. \tag{2}$$

In the above potential, all m_{11}^2, m_{22}^2, m_{12}^2 parameters as well as the λ_i ($i = 1, 2, 3, 4, 5$) couplings are assumed to be real to ensure that our potential is CP conserving. We also advocate a discrete Z_2 symmetry in order to avoid the flavor changing neutral currents (FCNC) at tree level. Such a Z_2 symmetry is only softly broken by the bilinear term proportional to m_{12}^2 parameter.

After electroweak symmetry breaking takes place, the outcome of the 8 degrees of freedom initially present in the two Higgs doublet fields: three are taken by the Goldstone bosons to give masses to the gauge bosons $W^\pm$ and Z, and five become the five physical Higgs states, including a pair of charged Higgs bosons, a CP-odd boson A, and two CP-even bosons: H and h with $m_h < m_H$. One of the neutral CP-even Higgs bosons would be identified as the 125 GeV Higgs-like particle observed at the LHC. The combination $v^2 = v_1^2 + v_2^2 = (2\sqrt{2}G_F)^{-1} = 4m_W^2/g^2$ can be used to fix one of the vacuum expectation values (VEVs) as a function of G_F and $\tan\beta$, together with the two minimization conditions, the scalar potential in Eq. (2) has seven independent parameters:

$$\alpha, \tan\beta = \frac{v_2}{v_1}, \qquad m_h = 125\ \text{GeV}, \qquad m_H, \qquad m_A, \qquad m_{H^\pm}, \quad \text{and} \quad m_{12}^2, \tag{3}$$

where α and β are, respectively, the CP-even mixing angle and CP-odd mixing angle. In this work, we consider h to be the SM-like boson observed at the LHC with $m_h = 125$ GeV, so the scalar potential is completely described by six independent parameters.

On the other hand, it is well known in the Yukawa sector that if we assume that both Higgs doublets couple to all fermions, we would end up with large tree-level FCNCs mediated by the neutral Higgs bosons. In order to avoid such large FCNCs, the 2HDM needs to satisfy the Paschos-Glashow-Weinberg theorem [51,52], which states that all fermions with the same quantum numbers can couple to the same Higgs doublet to avoid tree-level FCNCs. One can then have four different types (I, II, X, Y) of Yukawa textures. In the type-I model, only the second doublet Φ_2 interacts with all the fermions, while in the type-II model Φ_2 interacts with up-type quarks and Φ_1 interacts with the charged leptons and down-type quarks. The type-X model is where Φ_2 couples to all quarks and Φ_1 couples to all leptons, while in the type-Y (flipped) model the down-type quarks acquire masses from their couplings to Φ_1, and the charged leptons and up-type quarks couple to Φ_2.

In terms of the mass eigenstates of the neutral- and charged-Higgs boson fields, the Yukawa interactions can be written as

$$-\mathcal{L}_Y = \sum_{f=u,d,\ell}\frac{m_f}{v}\left[\kappa_h^f\bar{f}fh + \kappa_H^f\bar{f}fH - i\kappa_A^f\bar{f}\gamma_5 fA\right] + \frac{\sqrt{2}}{v}[\bar{u}_i V_{ij}(m_{u_i}\kappa_A^u P_L + \kappa_A^d m_{d_j}P_R)d_j H^+] + \frac{\sqrt{2}}{v}\bar{\nu}_L\kappa_A^\ell m_\ell \ell_R H^+ + \text{H.c.} \tag{4}$$

While the reduced couplings of the lighter Higgs boson, h, to either WW or ZZ are given by $\sin(\beta-\alpha)$, on the other hand, the couplings of the heavier Higgs boson, H, are equivalent to the SM couplings multiplied by $\cos(\beta-\alpha)$. Notably, the coupling between the pseudoscalar A and vector bosons is absent due to CP invariance.

Since throughout this study a few couplings are of crucial importance, we explicitly list the following identities:

$$\kappa_h^\ell(\text{II, X}) = -\frac{\sin\alpha}{\cos\beta} = s_{\beta-\alpha} - \tan\beta c_{\beta-\alpha}$$
$$\kappa_H^\ell(\text{II, X}) = \frac{\cos\alpha}{\cos\beta} = c_{\beta-\alpha} + \tan\beta s_{\beta-\alpha}.$$

It is clear that $-\frac{\sin\alpha}{\cos\beta}$ and $\frac{\cos\alpha}{\cos\beta}$ exhibit some enhancement for large $\tan\beta$. Note that close to the decoupling limit $\sin(\beta-\alpha)\approx 1$, which is also favored by LHC data, the h couplings to fermions reduce to unity.

For completeness, we also list the Feynman rules for pure scalar interactions:

$$
\begin{aligned}
g_{hH^+H^-} &= -\frac{1}{v}\left[(2m_{H^\pm}^2 - m_h^2)s_{\beta-\alpha} + \left(m_h^2 - 2\frac{m_{12}^2}{s_{2\beta}}\right)\frac{c_{\beta+\alpha}}{s_\beta c_\beta}\right] \\
g_{HH^+H^-} &= -\frac{1}{v}\left[(2m_{H^\pm}^2 - m_H^2)c_{\beta-\alpha} + \left(m_H^2 - 2\frac{m_{12}^2}{s_{2\beta}}\right)\frac{s_{\beta+\alpha}}{s_\beta c_\beta}\right] \\
g_{Hhh} &= -\frac{c_{\beta-\alpha}}{v s_{2\beta}^2}\left[(2m_h^2 + m_H^2)s_{2\alpha}s_{2\beta} - 2m_{12}^2(3s_{2\alpha} - s_{2\beta})\right] \\
g_{hH^+G^-} &= -\frac{c_{\beta-\alpha}}{v}(m_h^2 - m_{H^\pm}^2) \\
g_{HH^+G^-} &= -\frac{s_{\beta-\alpha}}{v}(m_H^2 - m_{H^\pm}^2).
\end{aligned} \tag{5}
$$

The relevant part of the Lagrangian describing the interactions of the gauge bosons with scalars is

$$
\begin{aligned}
\mathcal{L} = \frac{g}{2}W_\mu^+ &((H^- \overleftrightarrow{\partial}^\mu A) - ic_{\beta-\alpha}(H^- \overleftrightarrow{\partial}^\mu h) \\
&+ is_{\beta-\alpha}(H^- \overleftrightarrow{\partial}^\mu H)) + \text{H.c.} \\
&+ \frac{g}{2c_W}Z_\mu(c_{\beta-\alpha}(A \overleftrightarrow{\partial}^\mu h) - s_{\beta-\alpha}(A \overleftrightarrow{\partial}^\mu H)) \\
&+ \left(ie\gamma_\mu + i\frac{g(c_W^2 - s_W^2)}{2c_W}Z_\mu^+\right)(H^\mp \overleftrightarrow{\partial}^\mu H^\pm),
\end{aligned} \tag{6}
$$

where $\{s_W, c_W\} = \{\sin\theta_W, \cos\theta_W\}$ and θ_W stands for the Weinberg angle.

B. Theoretical and experimental constraints

There are both theoretical and experimental constraints that must be satisfied by the parameter space of the 2HDM. Theoretical constraints due to theoretical consistency conditions include vacuum stability, perturbative unitarity, and perturbativity. The experimental constraints include the measurements of Higgs boson properties, flavor-changing neutral current observables, and electroweak precision observables. These constraints play an important role in determining the allowed regions of the 2HDM parameter space and can guide the searches for new physics beyond the SM. So, we will provide a brief description of these constraints in this subsection.

(1) *Perturbative unitarity.* New physics beyond the SM must still obey the fundamental principles such as perturbative unitarity. Hence, in order to be consistent with such requirements within the 2HDM, one can impose perturbative unitarity in a variety of scattering processes among the various scalars and gauge bosons. These constraints have been taken from Refs. [53–55].

(2) *Perturbativity.* To avoid a nonperturbative theory, the quartic couplings of the scalar potential must obey the following conditions: $|\lambda_i| < 8\pi$ for each $i = 1, \ldots, 5$ [11].

(3) *Vacuum stability.* It is an important constraint that ensures the scalar potential to be bounded from below when the fields are allowed to take on larger and larger values. To fulfill this need, the Higgs potential must be positive in any direction of the fields Φ_i, and as a consequence the conditions [56,57],

$$
\lambda_{1,2} > 0, \quad \lambda_3 > -\sqrt{\lambda_1\lambda_2}, \quad \lambda_3 + \lambda_4 - |\lambda_5| > -\sqrt{\lambda_1\lambda_2} \tag{7}
$$

must be satisfied in the whole parameter space.

(4) *The EW precision observables.* These are utilized to quantify the deviations from the predictions of the SM. Those observables, namely S, T, and U [58], should be within 95% CL of their experimental measurements, and the current fit values are given by [59]

$$
\begin{aligned}
S &= 0.06 \pm 0.10, \quad T = 0.11 \pm 0.12, \\
U &= -0.02 \pm 0.09, \\
\rho_{ST} &= 0.90, \quad \rho_{SU} = -0.57, \quad \rho_{TU} = -0.82,
\end{aligned}
$$

where ρ_{ST} is the correlation parameter.

The constraints mentioned above have been incorporated into 2HDMC-1.8.0 [60], which is publicly available. This code is utilized to explore the parameter space of the 2HDM and assess its compatibility with the aforementioned constraints, as well as to calculate the Higgs branching ratios at each point. Additionally, 2HDMC includes an interface to HiggsBounds-5.10.1 [61,62] and HiggsSignals-2.6.1 [63], as described below.

(5) *BSM Higgs boson exclusions.* To make our study compatible with the existing exclusion limits at the 95% confidence level from Higgs searches at LEP, LHC, and Tevatron, we use the HiggsBounds-5.10.1 [61,62]. The primary search channels that have implications for the type-II and type-X 2HDM include

(a) Type-II
  (i) $pp \to A \to ZZ \to l^+l^+l^-l^-, l^+l^-qq, l^+l^-\nu\bar{\nu}$ [64].
  (ii) $bb \to A \to Zh \to l^+l^-bb$ [65].
  (iii) $pp \to A \to \tau^+\tau^-$ [66].
  (iv) $pp \to H \to \tau^+\tau^-$ [66].
  (v) $pp \to H \to ZZ \to l^+l^-l^+l^-, l^+l^-qq, l^+l^-\nu\bar{\nu}$ [64].
  (vi) $pp \to H \to VV$ [67].
  (vii) $pp \to A \to HZ \to b\bar{b}l^+l^-$ [68].
  (viii) $pp \to H \to AZ \to b\bar{b}l^+l^-$ [68].
  (ix) $gg \to A \to hZ \to b\bar{b}l^+l^-$ [69].

(b) Type-X
  (i) $gg \to A \to hZ \to b\bar{b}l^+l^-$ [69].
  (ii) $pp \to h \to \tau^+\tau^-$ [70].
  (iii) $pp \to H \to ZZ \to l^+l^-l^+l^-, l^+l^-qq, l^+l^-\nu\bar{\nu}$ [64].
  (iv) $gg \to A \to hZ \to b\bar{b}\tau^+\tau^-$ [71].
  (v) $pp \to A \to \tau^+\tau^-$ [66].
  (vi) $t \to H^+b \to \tau^+\nu b$ [72,73].
  (vii) $pp \to A \to \tau^+\tau^-$ [74,75].

TABLE II. Experimental results of $B_\mu \to \tau\nu$, $B^0_{s,d} \to \mu^+\mu^-$, and $\overline{B} \to X_s\gamma$ at 95% CL.

Observable	Experimental result	95% CL bounds
BR($B_\mu \to \tau\nu$) [92]	$(1.06 \pm 0.19) \times 10^{-4}$	$[0.68 \times 10^{-4}, 1.44 \times 10^{-4}]$
BR($B^0_s \to \mu^+\mu^-$) [92]	$(2.8 \pm 0.7) \times 10^{-9}$	$[1.4 \times 10^{-9}, 4.2 \times 10^{-9}]$
BR($B^0_d \to \mu^+\mu^-$) [86]	$(3.9 \pm 1.5) \times 10^{-10}$	$[0.9 \times 10^{-10}, 6.9 \times 10^{-9}]$
BR($\bar{B} \to X_s\gamma$) [92,93]	$(3.32 \pm 0.15) \times 10^{-4}$	$[3.02 \times 10^{-4}, 3.61 \times 10^{-4}]$

(viii) $gg \to A \to HZ \to \tau^+\tau^- l^+ l^-$ [76].
(ix) $pp \to H \to \tau^+\tau^-$ [66,74].
(x) $e^+e^- \to H^+H^- \to 4q, \tau^+\nu\tau^-\bar{\nu}$ [77].
(xi) $gg \to A \to hZ \to b\bar{b}l^+l^-$ [65].
(xii) $pp \to A \to HZ \to b\bar{b}l^+l^-$ [68].
(xiii) $pp \to H^+t\bar{b} \to \tau^+\nu t\bar{b}$ [72].
(xiv) $pp \to H \to hh \to \gamma\gamma b\bar{b}$ [78].
(xv) $pp \to H^+\bar{t}b \to t\bar{b}\,\bar{t}\,b$ [79].
(xvi) $pp \to h \to \tau^+\tau^-$ [74,75].
(xvii) $pp \to gg \to A \to \tau^+\tau^-$ [80].
(xviii) $pp \to H \to hZ \to \tau^+\tau^- l^+ l^-$ [71].
(xix) $pp \to A/VBF/WA/ZA/ttA \to \gamma\gamma$ [81].
(xx) $pp \to H \to hh \to b\bar{b}b\bar{b}$ [82].
(xxi) $pp \to H \to hh \to b\bar{b}/\tau^+\tau^-/W^+W^-/\gamma\gamma$ [83].
(xxii) $t \to H^+b \to c\bar{b}b$ [84].
(xxiii) $gg \to H \to t\bar{t}$ [85].

(6) *SM-like Higgs boson properties*. In the same vein, HiggsSignals-2.6.1 [63] is employed to check the compatibility of the SM-like scalar boson with the Higgs signal rate constraints from various searches and take into account the recent LHC 13 TeV results.
(7) *Flavor constraints*. This is related to the B-physics observables, and for this purpose we used the Superiso v4.1 tool [86] to calculate the relevant results. We then perform consistency checks at a 2σ CL, taking into account the available experimental measurements as reported in Table II.

III. COMPUTATIONAL PROCEDURE STEPS

In this section, we list all processes under investigation in this study. We give the contributing tree-level Feynman diagrams, their corresponding amplitudes, and the corresponding squares of amplitudes. We use the *Mathematica* packages, FeynArts [87] and FormCalc [88], to generate the amplitudes and to compute the corresponding cross sections. We also did a check of our calculation with FormCalc outputs and find perfect agreement.

A. Charged Higgs pair production

The tree-level Feynman diagrams contributing to $\mu^+\mu^- \to H^+H^-$ in the 2HDM are given in Fig. 1.

At tree level, the conventional Drell-Yan mechanism $\mu^+\mu^- \to \gamma^*, Z^* \to H^+H^-$ in Fig. 1 ($d_{3,4}$), the s-channel neutral-Higgs exchange $\mu^+\mu^- \to h^*, H^* \to H^+H^-$ in Fig. 1 ($d_{1,2}$), and the neutrino-exchange diagram in the t channel in Fig. 1 (d_5) all contribute to the process. The s-channel Higgs diagrams would be largely enhanced near the resonance region $\sqrt{s} \approx m_H$, while the t-channel diagram in Fig. 1 suffers from the Yukawa-coupling suppression at two vertices, but the large $\tan\beta$ value can give some amplification. If the Yukawa coupling of the charged Higgs to the muon becomes large, then it may give some enhancement for large center-of-mass energies.

We use $p_{1,2}$ for the momenta of the incoming μ^-, μ^+, and $k_{1,2}$ for the momenta of the outgoing charged Higgs bosons $H^\mp$. The four-momenta are defined in the center-of-mass system as

$$p_{1,2} = \left(\frac{\sqrt{s}}{2}, 0, 0, \pm\frac{\sqrt{s}}{2}\right)$$
$$k_{1,2} = \left(\frac{\sqrt{s}}{2}, \pm\frac{\sqrt{s}}{2}\beta_H \sin\theta, 0, \pm\frac{\sqrt{s}}{2}\beta_H \cos\theta\right), \quad (8)$$

where $\beta_H = \sqrt{1 - 4m^2_{H^\pm}/s}$, $\sqrt{s}$ is the center-of-mass energy, and θ is the scattering angle between μ^+ and H^+ in the center-of-mass frame. The Mandelstam variables s, t and u are defined by

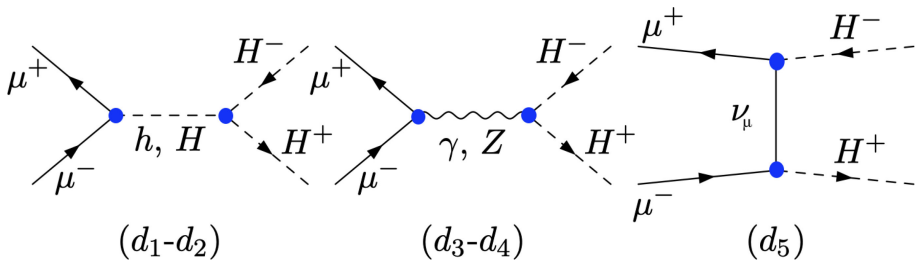

FIG. 1. Tree-level Feynman diagrams for H^+H^- at the muon collider in the 2HDM.

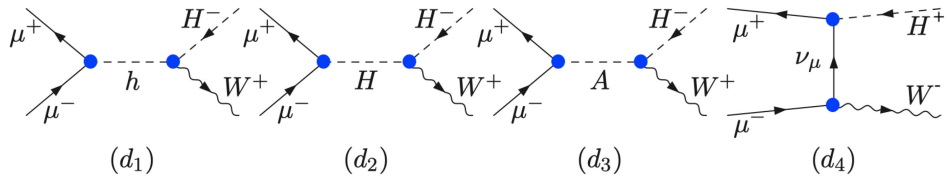

FIG. 2. Tree-level Feynman diagrams for $\mu^+\mu^- \to H^\pm W^\mp$ at the muon collider in the 2HDM.

$$
\begin{aligned}
s &= (p_1+p_2)^2 = (k_1+k_2)^2 \\
t &= (p_1-k_1)^2 = (p_2-k_2)^2 = m_{H^\pm}^2 - \frac{s}{2} + \frac{s}{2}\beta_H \cos\theta \\
u &= (p_1-k_2)^2 = (p_2-k_1)^2 = m_{H^\pm}^2 - \frac{s}{2} - \frac{s}{2}\beta_H \cos\theta. \qquad (9)
\end{aligned}
$$

Following the Feynman rules, the matrix elements for this process are given by

$$
\begin{aligned}
M_0^\gamma &= -2\frac{e^2}{s}\bar{v}(p_2)\not{k}_2 u(p_1) \\
M_0^z &= \frac{2g_H e^2}{s - m_Z^2 + i m_Z \Gamma_Z} \\
&\quad \times [g_V \bar{v}(p_2)\not{k}_2 u(p_1) - g_A \bar{v}(p_2)\not{k}_2 \gamma^5 u(p_1)] \\
M_0^\nu &= -\frac{g^2 m_\mu^2 \kappa_A^2}{4 m_W^2 t}(\bar{v}(p_2)\not{k}_2 u(p_1) + \bar{v}(p_2)\not{k}_2\gamma_5 u(p_1) \\
&\quad + m_\mu \bar{v}(p_2) u(p_1) + m_\mu \bar{v}(p_2)\gamma_5 u(p_1)) \\
M_0^{h_i} &= \bar{v}(p_2) u(p_1) \frac{g_{h_i H^+ H^-}}{s - m_{h_i}^2 + i m_{h_i}\Gamma_{h_i}} \frac{g m_\mu \chi_{h_i}^l}{2 m_W}, \qquad (10)
\end{aligned}
$$

where we have used the following couplings: $Z^\mu \mu^+ \mu^- = i\gamma^\mu(g_V - g_A\gamma^5)$ with $g_V = g(1-4s_w^2)/(4c_w)$ and $g_A = g/(4c_w)$. The Z coupling to a pair of charged Higgs is $g_H = -g(c_w^2 - s_w^2)/(2c_w)$.

We use the following notation:

$$
\begin{aligned}
Y_V &= -\frac{g^2 m_\mu^2 \kappa_A^2}{4 M_W^2} \\
a_h &= \frac{g_{hH^+H^-} g m_\mu \kappa_h^\ell}{2 M_W}, \qquad a_H = \frac{g_{HH^+H^-} g m_\mu \kappa_H^\ell}{2 M_W} \\
a_V &= -2\frac{e^2}{s} + \frac{2 g_H g_V}{s - M_Z^2 + i M_Z \Gamma_Z} + \frac{Y_V}{t} \\
a_A &= -\frac{2 g_H g_A}{s - M_Z^2 + i M_Z \Gamma_Z} + \frac{Y_V}{t} \\
a_S &= \frac{a_h}{s - M_h^2 + i M_h \Gamma_h} + \frac{a_H}{s - M_H^2 + i M_H \Gamma_H} + \frac{m_\mu Y_V}{t} \\
a_{SA} &= \frac{m_\mu Y_V}{t}, \qquad (11)
\end{aligned}
$$

where we have introduced the total width for the Z boson, h and H. The total widths for h and H are computed at the leading order. The inclusion of the total width is necessary for the case where the center-of-mass energy becomes close to the mass of the neutral-Higgs state: $\sqrt{s} \approx m_H$. The square of the amplitude is given by

$$
|M|^2 = \left[(|a_V|^2 + |a_A|^2)\frac{s^2}{2}\beta_H^2 \sin^2\theta + 2(|a_S|^2 - |a_{SA}|^2)s \right], \qquad (12)
$$

where we neglect the muon-mass term in M_0^ν amplitude. The differential cross section is given by

$$
\frac{d\sigma}{d\Omega} = \frac{\beta_H}{64\pi^2 s}\frac{1}{4}|M|^2. \qquad (13)
$$

The factor $1/4$ is due to initial state spin average. It is clear from above that the amplitude squared of the s-channel neutral-Higgs exchange does not depend on the scattering angle, therefore such contributions will have a flat angular distribution.

Note that in the case of the e^+e- collider, the s channel with h and H exchange and the t-channel neutrino exchange are neglected because of being proportional to the electron mass. The total cross section for $e^+e^- \to H^+H^-$ is given by [14]

$$
\sigma_{\rm tot}^{e^+e^-} = \frac{e^4 \pi \alpha^2 \beta_H^3}{3s}\left(1 + g_H^2 \frac{g_V^2 + g_A^2}{(1 - m_Z^2/s)^2} - \frac{2 g_H g_V}{1 - m_Z^2/s}\right). \qquad (14)
$$

B. $\mu^+\mu^- \to H^\pm W^\mp$ production

$\mu^+\mu^- \to H^\pm W^\mp$ is another process that could be important for the muon collider. Such a process may proceed via an s channel mediated by h, H or A in Fig. 2 $(d_{1,2,3})$ and by the neutrino-exchange t-channel diagram in Fig. 2 (d_4). This process may offer the following possible benefits (over the standard pair production discussed previously).

(i) The process $\mu^+\mu^- \to H^\pm W^\mp$ can provide information on the underlying Yukawa textures, since all the diagrams presented in Fig. 2 contain the muon coupling, in contrast to $\mu^+\mu^- \to H^+H^-$, which has an almost model-independent rate because it is mostly dominated by $\mu^+\mu^- \to \gamma^*, Z^* \to H^+H^-$, which depend only on the charged Higgs mass and gauge couplings.

(ii) Compared to charged-Higgs pair production, the production of a single $H^\pm$ is less constrained by the phase space, which further enables for a larger range of kinematics at a given center-of-mass energy, with on-shell production possible up to $\sim\sqrt{s}-M_W$.
(iii) The process may also experience resonance enhancement from the s-channel heavy-Higgs exchanges of H and A along the following pathways: $\mu^+\mu^- \to H^*, A^* \to H^\pm W^\mp$. Furthermore, this could be significant given that the coupling $W^\pm H^\mp A$ is a gauge coupling without any mixing suppression and $W^\pm H^\mp H$ is proportional to $\sin(\beta-\alpha)$, which is driven by the LHC data to its maximum value $\sin(\beta-\alpha)\approx 1$ [3,4].
(iv) The contribution from the t channel may be substantial regardless of whether $\sqrt{s}\approx M_{H,A}$ or not.

The kinematic for $\mu^+\mu^- \to H^\pm W^\mp$ is fixed as follows. The momenta of the incoming μ^+ and μ^-, the outgoing charged Higgs boson $H^\pm$, and the gauge boson $W^\mp$ are denoted by $p_{1,2}$ and $k_{1,2}$, respectively. Neglecting the muon mass m_μ, the momenta in the $\mu^+\mu^-$ center-of-mass system are given by

$$p_{1,2} = \frac{\sqrt{s}}{2}(1,0,0,\pm 1)$$
$$k_{1,2} = \frac{\sqrt{s}}{2}\left(1 \pm \frac{m_W^2 - m_{H^\pm}^2}{s}, \pm\frac{1}{s}\lambda^{\frac{1}{2}}(s, m_W^2, m_{H^\pm}^2)\sin\theta, 0, \pm\frac{1}{s}\lambda^{\frac{1}{2}}(s, m_W^2, m_{H^\pm}^2)\cos\theta\right).$$

Here $\lambda(x,y,z) = x^2+y^2+z^2-2xy-2xz-2yz$ is the usual two-body phase space function and θ is the scattering angle between μ^+ and H^+. The s, t, and u can be written as

$$\begin{aligned} s &= (p_1+p_2)^2 = (k_1+k_2)^2 \\ t &= (p_1-k_1)^2 = (p_2-k_2)^2 = \frac{1}{2}(m_W^2+m_{H^\pm}^2) - \frac{s}{2} + \frac{1}{2}\lambda^{\frac{1}{2}}(s, m_W^2, m_{H^\pm}^2)\cos\theta \\ u &= (p_1-k_2)^2 = (p_2-k_1)^2 = \frac{1}{2}(m_W^2+m_{H^\pm}^2) - \frac{s}{2} - \frac{1}{2}\lambda^{\frac{1}{2}}(s, m_W^2, m_{H^\pm}^2)\cos\theta \\ s+t+u &= m_W^2 + m_{H^\pm}^2. \end{aligned} \tag{15}$$

Similar to the first process, the s-channel $M_0^{h,H}$, M_0^A and t-channel M_0^ν amplitudes are respectively given by

$$\begin{aligned} M_0^h &= \frac{g^2 m_\mu}{4m_W}\frac{\cos(\beta-\alpha)\kappa_h^l}{s-m_h^2+im_h\Gamma_h}\bar{v}(p_2)u(p_1)(2k_1+k_2)^\mu\epsilon_\mu(k_2) \\ M_0^H &= \frac{g^2 m_\mu}{4m_W}\frac{-\sin(\beta-\alpha)\kappa_H^l}{s-m_H^2+im_H\Gamma_H}\bar{v}(p_2)u(p_1)(2k_1+k_2)^\mu\epsilon_\mu(k_2) \\ M_0^A &= \frac{g^2 m_\mu}{4m_W}\frac{-\kappa_A^l}{s-m_A^2+im_A\Gamma_A}\bar{v}(p_2)u(p_1)(2k_1+k_2)^\mu\epsilon_\mu(k_2) \\ M_0^\nu &= \frac{g^2 m_\mu}{2m_W}\frac{\kappa_A^l}{t}\bar{v}(p_2)\gamma^\mu\frac{1-\gamma_5}{2}(k_2-\not{p}_2)u(p_1)\epsilon_\mu(k_2). \end{aligned} \tag{16}$$

Taking into account the spin average of the initial state and polarization sum of the W gauge boson, the square of the amplitude is given by

$$|\mathcal{M}|^2 = \frac{sg^4m_\mu^2}{32m_W^4}\left[(|a_V|^2+|a_A|^2)\lambda(s, m_{H^\pm}^2, m_W^2) + 2a_t^2(2M_W^2p_T^2+t^2) + 2a_t(m_{H^\pm}^2m_W^2 - sp_T^2 - t^2)\Re(a_V-a_A)\right], \tag{17}$$

where $sp_T^2 = tu - m_W^2m_{H^\pm}^2 = \lambda(s, M_{H^\pm}^2, M_W^2)\sin^2\theta/4$, while the couplings a_V and a_A are given by

$$\begin{aligned} a_V &= \left(\frac{\cos(\beta-\alpha)\kappa_h^\ell}{s-m_h^2+im_h\Gamma_h} - \frac{\sin(\beta-\alpha)\kappa_H^\ell}{s-m_H^2+im_H\Gamma_H}\right) \\ a_A &= \frac{\kappa_A^\ell}{s-m_A^2+im_A\Gamma_A}; \qquad a_t = \frac{\kappa_A^\ell}{t}. \end{aligned} \tag{18}$$

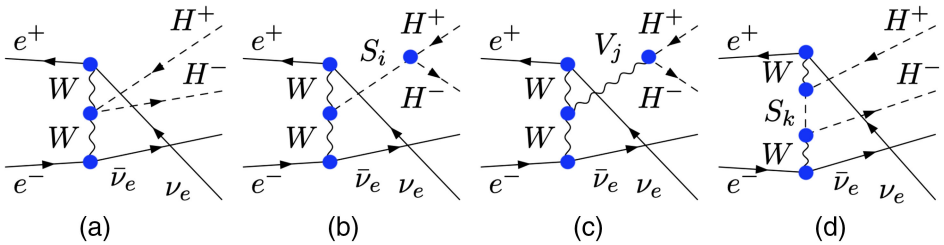

FIG. 3. Feynman diagrams involving dicharged Higgs production from VBF at the ILC: $e^+e^- \to \nu\bar{\nu}H^+H^-$. The contact channel contribution is represented in diagram (a), while the propagators S_i in diagram (b), V_j in diagram (c), and S_k in diagram (d) refer to (h, H), (γ, Z), and (h, H, A), respectively.

The differential cross section for $\sigma(\mu^+\mu^- \to H^\pm W^\mp)$ may be written as follows:

$$\frac{d\sigma}{d\Omega} = \frac{\lambda^{\frac{1}{2}}(s, m^2_{H^\pm}, m^2_W)}{64\pi^2 s^2}|\mathcal{M}|^2. \tag{19}$$

It is clear from the above amplitude squared of the s-channel neutral-Higgs exchange diagrams does not have any scattering angle dependence. Therefore, such s-channel Higgs-exchange diagrams will have a flat angular distribution.

C. Vector boson fusion (VBF)

Before ending this section, and in addition to the above, it is worth mentioning that vector boson fusion (VBF) processes, $e^+e^- \to \nu\bar{\nu}H^+H^-$, hold significant potential for producing charged Higgs bosons at electron-positron colliders, whether at the ILC with a center-of-mass energy of 500 GeV–1 TeV or at the CLIC with energies of 3, 6, and 10 TeV. While our initial analysis focused on the muon collider, we recognize that VBF processes could contribute significantly in certain scenarios. Specifically, the production of charged Higgs bosons alongside neutrinos via VBF in electron-positron collisions could occur at significant rates, depending on factors like collider energy and luminosity. The corresponding Feynman diagrams are shown in the Fig. 3.

IV. NUMERICAL RESULTS

We perform random scans over the parameter space of the 2HDM within the following ranges:

$$\begin{aligned} &m_h = 125.09\ \text{GeV}, \quad m_H \in [130, 1000]\ \text{GeV}, \\ &\sin(\beta-\alpha) \in [0.97, 1], \\ &m_{A,H^\pm} \in [80, 1000]\ \text{GeV}, \quad \tan\beta \in [0.5, 45], \\ &m^2_{12} \in [0, 1000^2], \end{aligned} \tag{20}$$

where we have assumed that the lightest Higgs state h is the observed SM-like Higgs boson at the LHC [1,2] and set $m_h = 125$ GeV. After scrutinizing the parameter space of the model with the theoretical and experimental constraints described above, the resulting parameter space points will be passed to FormCalc [88–90] to compute the corresponding cross section of each process at the muon collider.

In the plane $[m_A, m_{H^\pm}]$, we illustrate the mass splitting between m_H and m_A in Fig. 4(a) and between $m_{H^\pm}$ and m_H in Fig. 4(b), while Fig. 4(c) exhibits the correlation between m_H and m^2_{12}. It is clear that, for $m_{H^\pm} \leq 600$ GeV, the splitting between A and H could be quite large while, for

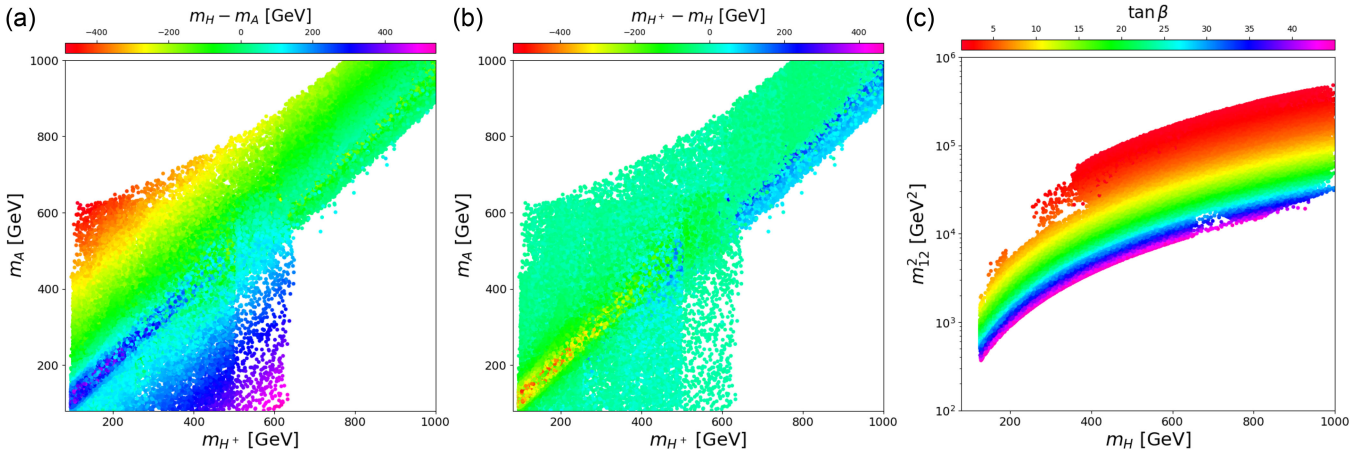

FIG. 4. Correlations between m_A and $m_{H^\pm}$ (a and b) and between m^2_{12} and m_H (c) after imposing the theoretical and experimental constraints. The color code indicates the splitting $m_H - m_A$, $m_{H^+} - m_H$, and $\tan\beta$, respectively.

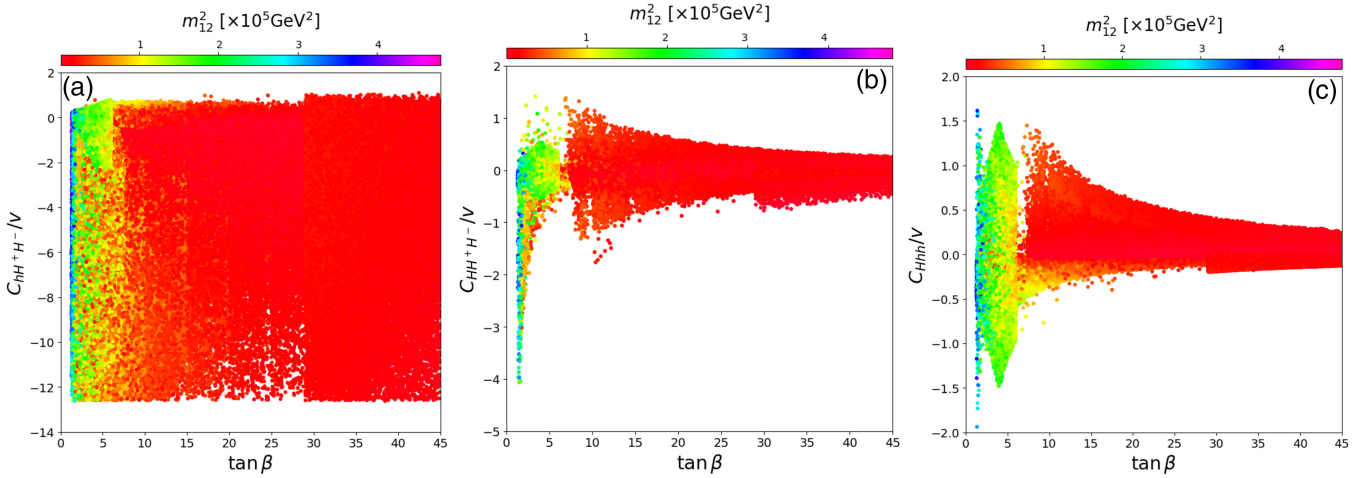

FIG. 5. Pure scalar couplings normalized to the SM VEV v as a function of $\tan\beta$: (a) $g_{hH^+H^-}/v$, (b) $g_{HH^+H^-}/v$, and (c) g_{Hhh}/v with m_{12}^2 represented by the color code.

$m_{H^\pm} \geq 600$ GeV, the splitting between the charged Higgs and neutral heavy states H and A becomes rather small. In Fig. 4(c) we show the correlation between m_H and m_{12}^2, as we know the mass of the heavy states H, A, and $H^\pm$ are driven by m_{12}^2 [91]:

$$m_{H,A,H^\pm}^2 \approx \frac{m_{12}^2}{s_\beta c_\beta} + \lambda_i v^2 + \mathcal{O}(v^4/m_{12}^2). \tag{21}$$

In order to have m_H of the order of 1 TeV, a large $m_{12}^2 \geq 3\times 10^4$ GeV^2 is needed.

In Fig. 5, we illustrate the pure scalar couplings normalized to the VEV as functions of $\tan\beta$. In panels (a), (b), and (c), one can see the allowed size for $g_{hH^+H^-}/v$, $g_{HH^+H^-}/v$, and g_{Hhh}/v, respectively. To understand this behavior, we give the couplings $g_{hH^+H^-}$, $g_{HH^+H^-}$, and g_{Hhh} of Eq. (5) in the alignment limit $\sin(\beta-\alpha)\approx 1$ ($\beta \approx \alpha + \pi/2$) as

$$\begin{aligned} g_{hH^+H^-} &= -\frac{1}{v}\left[2m_{H^\pm}^2 + m_h^2 - 2\frac{m_{12}^2}{s_\beta c_\beta}\right] \\ g_{HH^+H^-} &= -\frac{1}{v}\left[-\left(m_H^2 - \frac{m_{12}^2}{s_\beta c_\beta}\right)\frac{\cos(2\beta)}{s_\beta c_\beta}\right] \\ g_{Hhh} &= -\frac{c_{\beta-\alpha}}{v}\left[-(2m_h^2 + m_H^2) + 4\frac{m_{12}^2}{s_\beta c_\beta}\right]. \end{aligned} \tag{22}$$

Further in the large $\tan\beta$ limit, we have $1/(s_\beta c_\beta) \approx \tan\beta + \mathcal{O}(\frac{1}{\tan\beta})$, $\cos(2\beta)/(s_\beta c_\beta) \approx -\tan\beta + \mathcal{O}(\frac{1}{\tan\beta})$, and $\cos(2\beta)/(s_\beta^2 c_\beta^2) \approx -\tan^2\beta + \mathcal{O}(\frac{1}{\tan^2\beta})$, therefore,

$$\begin{aligned} g_{hH^+H^-} &\approx -\frac{1}{v}\left[2m_{H^\pm}^2 + m_h^2 - 2m_{12}^2\left(\tan\beta + \mathcal{O}\left(\frac{1}{\tan\beta}\right)\right)\right] \\ g_{HH^+H^-} &\approx -\frac{1}{v}\left[-m_H^2\left(-\tan\beta + \mathcal{O}\left(\frac{1}{\tan\beta}\right)\right)\right. \\ &\quad \left. + m_{12}^2\left(-\tan^2\beta + \mathcal{O}\left(\frac{1}{\tan^2\beta}\right)\right)\right] \end{aligned} \tag{23}$$

$$g_{Hhh} \approx -\frac{c_{\beta-\alpha}}{v}\left[-(2m_h^2 + m_H^2) + 4m_{12}^2\tan\beta + \mathcal{O}\left(\frac{1}{\tan^2\beta}\right)\right]. \tag{24}$$

It is evident that both $g_{hH^+H^-}$ and g_{Hhh} have partial linear dependence on $\tan\beta$, while $g_{HH^+H^-}$ has both partially linear and quadratic dependence on $\tan\beta$. However, this $\tan\beta$ dependence will eventually cancel out, because both m_H and $m_{H^\pm}$ are given by $\frac{m_{12}^2}{s_\beta c_\beta} \approx m_{12}^2\tan\beta$ in the large m_{12}^2 limit. This cancellation is more pronounced for $g_{HH^+H^-}$ and g_{Hhh} couplings, where it can be observed that, for large $\tan\beta$, the $g_{HH^+H^-}$ and g_{Hhh} couplings become small.

(i) $\mu^+\mu^- \to H^+H^-$.

The key results of our investigation for the muon collider with center-of-mass energy of 3 TeV are illustrated in Fig. 6 for charged-Higgs pair production. For such a process, we first point out that, because the dominant contribution comes from the s-channel $\mu^+\mu^- \to \gamma, Z \to H^+H^-$ diagrams [Fig. 1 ($d_{3,4}$)], the cross section is exactly the same as one can obtain via $e^+e^- \to H^+H^-$ at e^+e^- colliders at the same $\sqrt{s}$. In additional, we have the s-channel neutral-Higgs exchange $\mu^+\mu^- \to h, H \to H^+H^-$ [Fig. 1 ($d_{1,2}$)], which is in general smaller than $\mu^+\mu^- \to \gamma, Z \to H^+H^-$. The t-channel contribution is rather suppressed by m_μ^4. We stress here that the interference between $\mu^+\mu^- \to \gamma, Z \to H^+H^-$ and $\mu^+\mu^- \to h, H \to H^+H^-$ is constructive, resulting in a

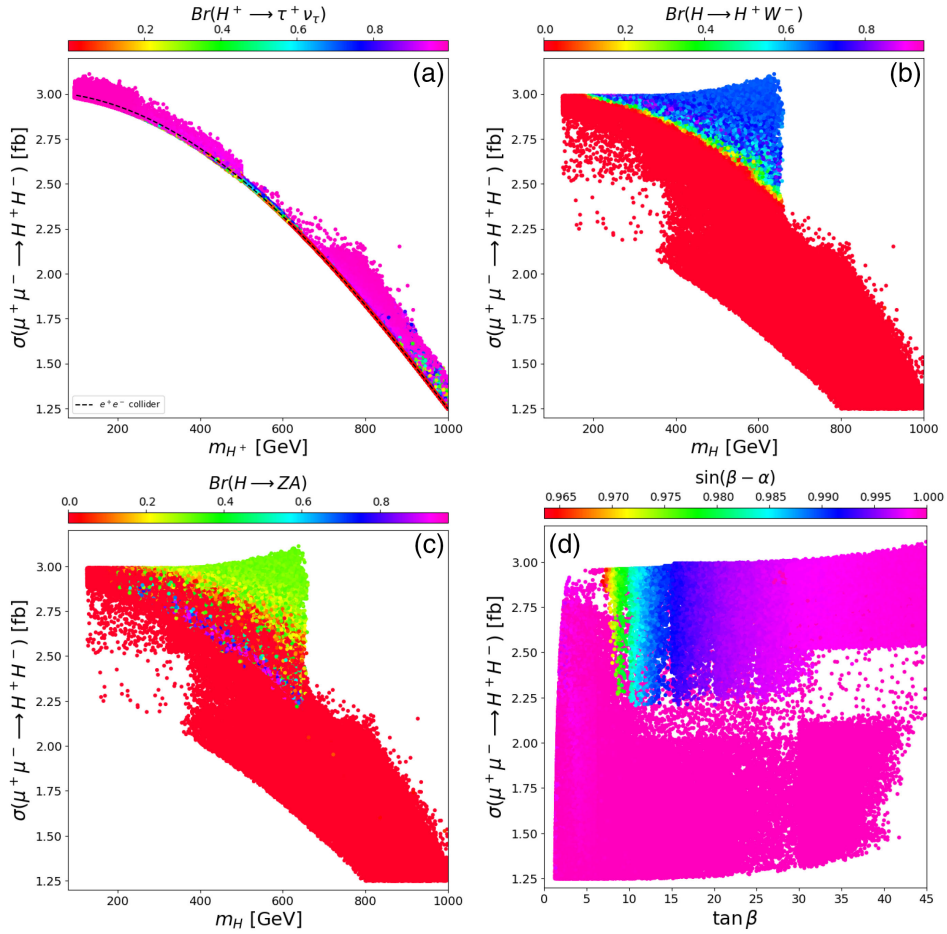

FIG. 6. Production cross sections for $\mu^+\mu^- \to H^+H^-$ in type X as a function of $m_{H^\pm}$ (a), m_H (b and c) and $\tan\beta$ (d) at $\sqrt{s} = 3$ TeV. The color legend presents respectively the following observables: $\sin(\beta-\alpha)$, $\mathrm{Br}(H^+ \to \tau^+\overline{\nu_\tau})$, $\mathrm{Br}(H \to H^\pm W^\mp)$, and $\mathrm{Br}(H \to ZA)$. All of the regions are consistent with theoretical and experimental constraints.

cross section that is all times larger than the corresponding $\sigma(\mu^+\mu^- \to \gamma, Z \to H^+H^-) = \sigma(e^+e^- \to H^+H^-)$.

The panels in Fig. 6 show the correlations between the production cross section $\sigma(\mu^+\mu^- \to H^\pm H^\mp)$ and m_H, $m_{H^\pm}$, and $\tan\beta$ for $\sqrt{s} = 3$ TeV.

The cross section is slightly improved overall in the permitted dataset. It can reach a maximum value up to ~3.2 fb for low $m_{H^\pm}$ however large $\tan\beta$. Keep in mind that the 2HDM type II and type X (or type III) are both affected by the enhancement for large $\tan\beta$ (see Table I for the couplings). We also see that, as supported by the LHC data, the maximal cross section is found for $\sin(\beta-\alpha) \approx 1$. From the plots in Figs. 6(b) and 6(c), one can clearly see the large rise in the total cross section, which corresponds to the large $\tan\beta$ from the s-channel contribution $\mu^+\mu^- \to H^* \to H^+H^-$ when $H\mu^+\mu^-$ receives significant $\tan\beta$ amplification.

Furthermore, it can be observed from Fig. 6(a) that, most of the time, there is constructive interference between the (γ, Z) s-channel and (h, H) s-channel contributions, since the cross section for $\mu^+\mu^- \to H^+H^-$ is greater than $e^+e^- \to H^+H^-$. However, such interference could also be destructive, as seen in a small region of the parameter space in Fig. 6(a) below the dashed line, where $\mu^+\mu^- \to H^+H^-$ is smaller compared to $e^+e^- \to H^+H^-$.

Additionally, the maximum enhancement is achieved for the neutral-Higgs mass M_H in the region of [500, 650] GeV and the highest allowable $\tan\beta \approx 45$. Here, we emphasize that the theoretical and experimental constraints still permit $\tan\beta \geq 45$ for 2HDM type X, suggesting that the cross section may be a little larger than what we show. We only scan up to $\tan\beta \leq 45$ in our study due to time constraints. The cross section $e^+e^- \to H^+H^-$ starts to become suppressed in the range $m_{H^\pm} \in [200, 250]$ GeV due to phase space suppression, see Fig. 6(a) (dashed line). As a result, the muon collider can be used in addition to e^+e^- machines to study the region of the parameter space that the linear collider is unable to access.

The CP-even Higgs can decay into $b\bar{b}$, $\tau^+\tau^-$, WW, ZZ, $t\bar{t}$, ZA, hh, $W^\pm H^\mp$, and H^+H^-. In the 2HDM type X, $H \to \tau^+\tau^-$ would be the dominant decay mode at large $\tan\beta$.$H \to WW, ZZ$ are suppressed since both are

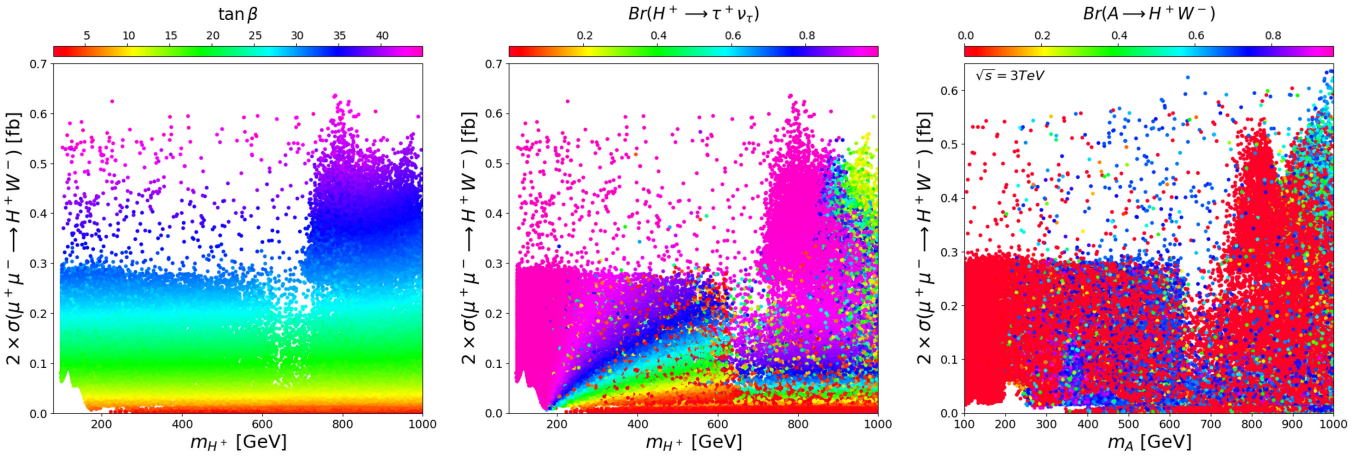

FIG. 7. Production cross sections for $\mu^+\mu^- \to W^\pm H^\mp$ in type X as a function of $m_{H^\pm}$ (left and middle panels) and m_A (right panel), at $\sqrt{s} = 3$ TeV. The color legend presents, respectively, the following parameter/observables: $\tan\beta$, $\mathrm{Br}(H^+ \to \tau^+\bar{\nu})$, and $\mathrm{Br}(A \to H^\pm W^\mp)$. All of the regions are consistent with theoretical and experimental constraints.

proportional to $\cos(\beta-\alpha) \approx 0$, but nevertheless they could reach a few percent branching fraction in some cases. After crossing the $t\bar{t}$ threshold, there is a strong competition between hh, ZA, $W^\pm H^\mp$, and H^+H^-. The decay channel $H \to H^+H^-$, which is open only for $m_H > 2m_{H^\pm}$, is rather small compared to $H \to W^\pm H^\mp$ and $H \to ZA$, which have more phase space and the coupling $HW^\pm H^\mp, HZA \propto \sin(\beta-\alpha)$ is maximal and this makes the $\mathrm{Br}(H \to W^\pm H^\mp)$ and $\mathrm{Br}(H \to ZA)$ rather substantial as can be seen from Figs. 6(b) and 6(c). Therefore, since $\mathrm{Br}(H \to H^+H^-)$ is very small, the cross section $\sigma(\mu^+\mu^- \to H^* \to H^+H^-)$ is not strongly enhanced because $\sigma(\mu^+\mu^- \to H^* \to H^+H^-) \approx \sigma(\mu^+\mu^- \to H) \times \mathrm{Br}(H \to H^+H^-)$. On the other hand, one would expect that the cross section $\sigma(\mu^+\mu^- \to W^\pm H^\mp)$ would receive significant enhancement.

In Fig. 6, one can also read branching fractions of $H^\pm$. For $m_{H^+} \equiv 86$–120 GeV, the decay mode $H^+ \to \tau\nu_\tau$ dominates. However, as m_{H^+} gets larger, e.g. $m_{H^+} \geq 175$ GeV, a significant competition arises among the decay modes $H^+ \to t\bar{b}$, $H^+ \to W^+A$, $H^+ \to W^+h$, and $H^+ \to W^+H$.

It is evident that as the center-of-mass energy grows from $\sqrt{s} = 3$ to 10 TeV, the cross section reduces considerably. The cross section is dominated by the s-channel diagrams $\mu^+\mu^- \to \gamma, Z \to H^+H^-$ and $\mu^+\mu^- \to h, A \to H^+H^-$, both of which behave like $1/s$. Note that at these center-of-mass energies, the cross section $\mu^+\mu^- \to H^+H^-$ is fully dominated by the s-channel γ and Z boson exchanges while the s-channel Higgs exchange is much smaller than the other two, except near the charged Higgs pair production threshold, where both s channels become comparable. For the charged-Higgs mass increase from 250 GeV to 1 TeV and small $\tan\beta$, the cross section decreases from 3 to 1.5 fb. The muon coupling to the neutral Higgs bosons h, H can increase the cross section for large $\tan\beta$.

(i) $\mu^+\mu^- \to H^\pm W^\mp$.

The other part of our investigation for the muon collider at $\sqrt{s} = 3$ TeV is illustrated in Fig. 7 for the associate production of a charged Higgs with W. Unlike $\mu^+\mu^- \to H^\pm H^\mp$, the present process is insensitive to the pure scalar couplings due to the presence of W in the final state. In addition, the s-channel diagram with the exchange of h is suppressed by $hW^\pm H^\mp \propto \cos(\beta-\alpha) \approx 0$, while the s-channel diagrams with H and A exchanges will benefit from an enhancement since $HW^\pm H^\mp$ is proportional to $\sin(\beta-\alpha) \approx 1$ while $AW^\pm H^\mp$ is a pure gauge coupling without any mixing factor.

Unlike $\mu^+\mu^- \to H^\pm H^\mp$, the t-channel contribution for $\mu^+\mu^- \to W^\pm H^\mp$ with neutrino exchange is smaller than the s-channel contribution involving the neutral-Higgs exchanges but is not negligible. In the case of $\mu^+\mu^- \to H^\pm H^\mp$, the t-channel amplitude is proportional to m_μ^2, while for $\mu^+\mu^- \to W^\pm H^\mp$ the t-channel amplitude has only one m_μ suppression which could overcome with the large $\tan\beta$ value. Therefore, both the t- and s-channel contributions are proportional to $\tan\beta$ in the large $\tan\beta$ limit, since both $H\mu^+\mu^- \propto c_\alpha/c_\beta \approx c_{\beta-\alpha} + \tan\beta s_{\beta-\alpha} \approx \tan\beta$. In the large $\tan\beta$ limit, the amplitudes of all diagrams are proportional to $\tan\beta$, therefore we would expect enhancement for large $\tan\beta$ for both type II and type X.

Let us recall that the CP-odd boson A can decay into $b\bar{b}$, $\tau^+\tau^-$, $t\bar{t}$, Zh, ZH, and $W^\pm H^\pm$. Because of CP invariance, A does not couple to WW and ZZ. Before the opening of the $t\bar{t}$ threshold, the CP-odd A would decay dominantly into $\tau^+\tau^-$ and $b\bar{b}$ with a preference into $\tau^+\tau^-$ for large $\tan\beta$, while for $m_A > 2m_t$ there will be a strong competition between $A \to t\bar{t}$, $A \to \tau^+\tau^-$, $A \to ZH$, and $A \to W^\pm H^\pm$ channels since $A \to Zh$ is proportional to $\cos(\beta-\alpha) \approx 0$ while $A \to t\bar{t}$ is proportional to $1/\tan\beta$ which is suppressed for large $\tan\beta$ limit. As the plots indicate, $\mathrm{Br}(A \to W^\pm H^\mp)$ is the dominant one and could exceed 70%. The possible decays of H have been discussed above.

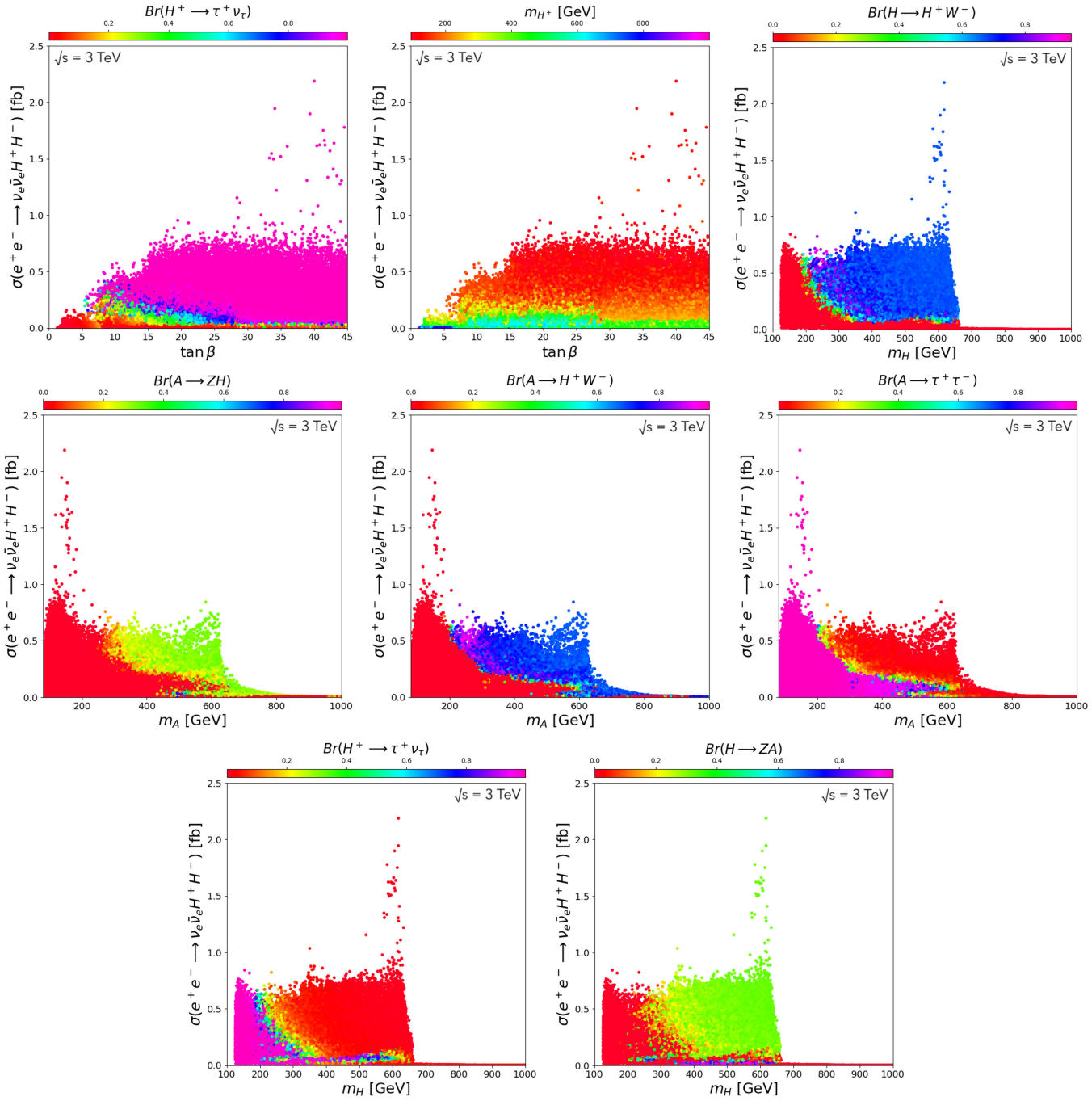

FIG. 8. Production cross sections for $e^+e^- \to \nu_e\bar{\nu}_e H^+H^-$ in type X as a function of the model parameters, at the Compact Linear Collider (CLIC) with the center-of-mass energy of $\sqrt{s} = 3$ TeV. The color legend presents one of the following observables: $m_{H^\pm}$, $\mathrm{Br}(H^+ \to \tau^+\bar{\nu}_\tau)$, $\mathrm{Br}(H \to H^\pm W^\mp, ZA)$ and $\mathrm{Br}(A \to ZH, H^\pm W^\mp, \tau^+\tau^-)$. All of the regions are consistent with theoretical and experimental constraints.

The production cross sections for 3 TeV are depicted in Fig. 7. The cross section for $\mu^+\mu^- \to W^\pm H^\mp$ is slightly lower than $\mu^+\mu^- \to H^\pm H^\mp$. The difference could be attributed to the wider range of kinematics inherent in this process at a given $\sqrt{s}$. As expected, the cross section raises and is of the order of 0.63 fb for large value of $\tan\beta$. Also, one can see a large $\mathrm{Br}(A \to H^\pm W^\mp)$ effect from $\mu^+\mu^- \to A^* \to W^\pm H^\mp$, which could enhance the cross section while $\mathrm{Br}(H \to W^\pm H^\mp)$ is rather small of the order 10^{-3}. The competition between $H \to hh$, $H \to \tau^+\tau^-$, and $H \to ZA$ which makes $\mathrm{Br}(H \to W^\pm H^\mp)$ rather suppressed. One can see from the figures, the maximum cross section for $\mu^+\mu^- \to W^\pm H^\mp$ could reach more that 0.63 fb.

(i) $e^+e^- \to \nu_e\bar{\nu}_e H^+H^-$.

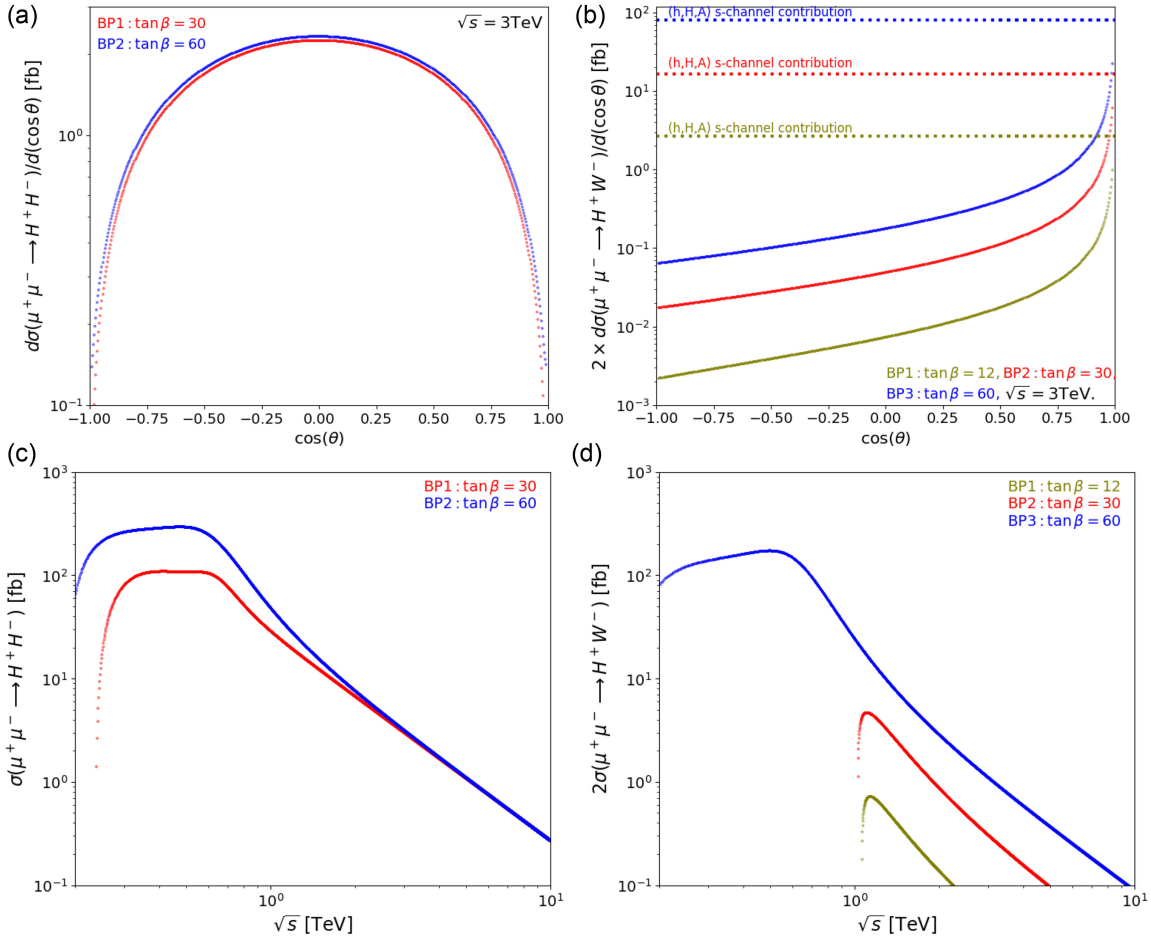

FIG. 9. Angular distribution for $\mu^+\mu^- \to H^\pm H^\mp$ (a) and $\mu^+\mu^- \to H^\pm W^\mp$ (b) as a function of $\cos\theta$ at $\sqrt{s} = 3$ TeV for the two benchmark points. Total cross section for $\mu^+\mu^- \to H^\pm H^\mp$ (c) and $\mu^+\mu^- \to H^\pm W^\mp$ (d) as a function of $\sqrt{s}$ for the selected benchmark points. Note that $e^+e^- \to H^\pm W^\mp$ is loop suppressed.

Figure 8 illustrates our findings regarding the associated pairwise production of dicharged Higgs bosons with ν_e, highlighting a strong dependence of the cross section on the model parameters. Hence, a significant variation in the production cross section may occur, especially when the charged Higgs boson is relatively light and decays mainly to $\tau^\pm\bar{\nu}_\tau$. The CP-even H exchange, as depicted in Fig. 3(b) or 3(d), contributes significantly for m_H around 600 GeV. Conversely, the CP-odd Higgs boson, A, may both improve the cross section and give rise to $\tau^+\tau^-$ for $m_A \leq 200$ GeV. However, for the muon collider context, while the new channels we highlighted in our study alter the landscape of potential production mechanisms, the impact of VBF processes warrants further investigation. Moving forward, we aim to extend our analysis to include a more comprehensive evaluation of VBF contributions in both e^+e^- and muon collider setups, thereby enhancing our understanding of charged Higgs boson production in these environments.

We illustrate the angular distribution $d\sigma/d\cos\theta$ for both processes in Figs. 9(a) and 9(b) for selected benchmark points: $\tan\beta = 12$, $\tan\beta = 30$, and $\tan\beta = 60$ at $\sqrt{s} = 3$ TeV (see Table III). It is evident that for H^+H^- pair production, the distribution remains symmetric about $\cos\theta = 0$. Such a distribution depends solely on the exchanges of γ and Z in the s channel. For the s-channel h and H contributions, the angular distribution tends to be flat due to the absence of scattering-angle dependence. Evidently, the angular distribution at the muon collider is the same as for $e^+e^- \to H^+H^-$, except that it is slightly shifted by the contributions of the scalar h and H exchanges, which can nevertheless significantly improve the cross-section production by several orders of magnitude for $\tan\beta = 60$.

In Fig. 9(b), we display the differential cross section for $\mu^+\mu^- \to H^+W^-$. This includes both the flat differential distribution of the s-channel contributions $\mu^+\mu^- \to h^*, H^*, A^* \to W^\pm H^\mp$, as well as the total angular distribution from both the s-channel and t-channel contributions. It is clear that destructive interference occurs between s- and t-channel contributions, leading to suppressed total cross sections. Notably, an enhancement near the forward direction ($\cos\theta \approx 1$) can be seen due to the t-channel singularity.

Figures 9(c) and 9(d) present the total cross sections for both processes at e^+e^- and $\mu^+\mu^-$ colliders as a function of $\sqrt{s}$ for various values of $\tan\beta$. For both processes, we select benchmark points to highlight the resonance effect from the s-channel H contribution. In the case of $\sigma(\mu^+\mu^- \to H^+H^-)$, such resonance effects are amplified with large $\tan\beta$. At higher energy $\sqrt{s} > 2$ TeV, the cross section for $\sigma(\mu^+\mu^- \to H^+H^-)$ exhibits no $\tan\beta$ dependence and is fully dominated by the γ and Z exchanges. For comparison we also show the angular distribution for $e^+e^- \to H^+H^-$ at $\sqrt{s} = 1$ TeV and for charged Higgs mass as specified for $\mathrm{BP}_{1,2}$. Similarly, in the case of $\sigma(\mu^+\mu^- \to H^\pm W^\mp)$, one can see the resonance effect from the H exchange. Because of the destructive interference between the s-channel and t-channel contributions, one can see a quick drop of the cross section as a function of $\sqrt{s}$.

Implicitly, the $\sigma(\mu^+\mu^- \to H^\pm W^\mp)$ depends both on the energy of the muon collider as well as $\tan\beta$, unlike the H^+H^- production mode where the total cross section drastically decreases for high $\sqrt{s}$ values and becomes insensitive to $\tan\beta$. Furthermore, contrary to $\sigma(\mu^+\mu^- \to H^+H^-)$, the fact that the amplitude of $\mu^+\mu^- \to H^\pm W^\mp$ proportional to $\tan\beta$ results in a clear shift between BP_1 for $\tan\beta = 30$ and BP_2 for $\tan\beta = 60$ can be seen from Fig. 9(d). Note that $e^+e^- \to H^\pm W^\mp$ is loop suppressed and thus not shown here.

At the end of this section, we stress that all the results displayed above are for 2HDM type X. Since all of the neutral and charged Higgs couplings to the muons involved are the same in type II and type X, we would get the same numerical result for the same set of parameters for 2HDM type II. The same statement is true for 2HDM types I and Y. The parameter space for the 2HDM type II is constrained in two ways. The first comes from B-physic observables, as noted by [92,93]. The most demanding requirement comes from $\bar{B} \to X_s\gamma$, which demands that the charged Higgs boson be heavier than 680 GeV [94–96]. The second restriction is caused by LHC data which requires $\tan\beta \leq 12$. As a result, the production of charged Higgs pairs is only possible for large center of mass energies $\sqrt{s} \geq 1360$ GeV, and in such a circumstance, the s-channel neutral Higgs contribution is largely suppressed. In this scenario, the cross section would resemble $\sigma(e^+e^- \to H^+H^-)$ given in Eq. (14). In the case of $\mu^+\mu^- \to W^\pm H^\mp$ in the 2HDM type X, for charged Higgs heavier than 680 GeV and $\tan\beta < 12$, at $\sqrt{s} =$ 1 TeV the maximum cross section one can get is about a few fb. This cross section is even reduced for $\sqrt{s} \geq 1$ TeV.

However, the resulting cross section for $\mu^+\mu^- \to H^+H^-$ in the 2HDM type I and Y does not yield any meaningful results. This outcome results from the fact that the couplings $\xi_H^\ell = s_\alpha/s_\beta \propto 1/\tan\beta$ are suppressed for large $\tan\beta$ and the coupling ξ_h^ℓ reduces to unity. Therefore, the primary component of the cross section arises from the $\mu^+\mu^- \to \gamma^*, Z^* \to H^+H^-$ given in Eq. (14). The same thing can be said for the $\sigma(\mu^+\mu^- \to H^\pm W^\mp)$ cross section which is proportional to $1/\tan^2\beta$ at the large $\tan\beta$ limit and is therefore small.

V. SIGNAL VS BACKGROUND ANALYSIS

A. Monte Carlo toolchain

This study for the future muon collider operating at $\sqrt{s} = 3$ TeV focuses on the final state, which consists of a pair of tau leptons plus missing energy through the decay mode $\mu^+\mu^- \to H^+H^- \to \tau_h^+\nu\tau_h^-\nu$, VBF channel, and $\mu^+\mu^- \to H^+W^- \to W^+W^-h \to \tau_h^+\nu\tau_h^-\nu$. For each channel, we adopt the benchmarks set in Table IV.

To simulate the signal events, we generate the parton-level processes using MadGraph5_aMC_v3.4.1 [97]. Event samples are then interfaced with PYTHIA-8.20 [98] for fragmentation and showering, and subsequently processed through the DELPHES-3.4.5 [99] for detector simulation, where we use the muon collider Detector TARGET model. Jets are clustered using the anti-k_t [100] algorithm through DELPHES with a jet radius $R = 0.5$. At the DELPHES level, we first require that the candidate for a b jet should pass the minimal acceptance of $p_T > 20$ GeV. Then we apply the b-tagging efficiency about 70% and the mistag rates of the charm or light quark jet as a b jet as a function of pseudorapidity and energy. To assess the observability, we evaluate the statistical significance (S) using the formula:

$$S = \sqrt{\mathcal{L}}\frac{\sigma_s}{\sqrt{\sigma_s + \sigma_b}}, \tag{25}$$

TABLE III. The benchmark points (BPs) selected in type X of the 2HDM for differential cross sections.

Parameters	m_h	m_H	m_A	$m_{H^\pm}$	$\sin(\beta-\alpha)$	$\tan\beta$	m_{12}^2 (GeV^2)	$\sigma_{Muon}^{3\,\mathrm{TeV}}$ (fb)	$\sigma_{LHC}^{14\,\mathrm{TeV}}$ (fb)
Processes: Charged Higgs pair production									
BP1	125.09	598.13	148.36	119.1	0.9977	30	11873.03	3.001	117.6
BP2	125.09	509.68	102.52	95.11	0.9994	60	4328.42	3.15	258.1
Processes: Associate production									
BP1	125.09	801.87	973.69	980.04	0.9999	12	53003.52	0.048	5.619×10^{-3}
BP2	125.09	737.76	904.88	946.1	0.9999	30	18086.76	0.304	1.062×10^{-3}
BP3	125.09	509.68	102.52	95.11	0.9994	60	4328.42	1.1	12.37

TABLE IV. The description of our BPs.

	Signal	m_h	m_H	m_A	$m_{H^\pm}$	$\tan\beta$	$\sin(\beta-\alpha)$	m_{12}^2
BP1	$\tau_h^+\nu\tau_h^-\nu$	125.09	590.5	234.04	207.28	44.63	0.9990	7808.71
BP2	VBF	125.09	622.39	267.96	248.14	32.18	0.9981	12025.25
BP3	$\tau_h^+\nu\tau_h^-\nu$	125.09	608.51	166.7	162.7	28.57	0.9977	12942.8

where σ_s and σ_b are the signal and background cross sections after all the cuts and $\mathcal{L}$ is the integrated luminosity.

B. $\mu^+\mu^- \to H^+H^-$ and VBF production

Production of a pair of charged-Higgs bosons is considered to be one of the most challenging processes at the LHC. In this subsection, we focus on pair production of charged Higgs at future muon collider and VBF production with the final state $\tau^+\nu\tau^-\nu$:

$$\mu^+\mu^- \to H^+H^- \to \tau_h^+\nu\tau_h^-\nu.$$

To search the signals against the SM background, we present the main SM backgrounds, which include top-pair production $t\bar{t}$, diboson production $VV = WW = ZZ$, Zjj, and Wjj listed below.

(i) $\mu^+\mu^- \to t\bar{t}$.
(ii) $\mu^+\mu^- \to VV$.
(iii) $\mu^+\mu^- \to Z/\gamma jj$ with $Z \to \tau\tau$ and $Z \to \nu\nu$.
(iv) $\mu^+\mu^- \to Wjj$ where one τ_h comes from W decay and the other τ_h from a jet misidentified as τ_h.

To ensure that the parton-level events meet the required criteria, we impose $p_T^j > 25$ and $|\eta_j| < 2.5$ on jets. However, at DELPHES level we employ the τ-tagging efficiencies and the mistag rates of a light jet as $\tau P_{\tau\to\tau} = 0.85$ and $P_{j\to\tau} = 0.02$, respectively. Furthermore, we apply the charged lepton identification and typical photon isolation criteria, where we require

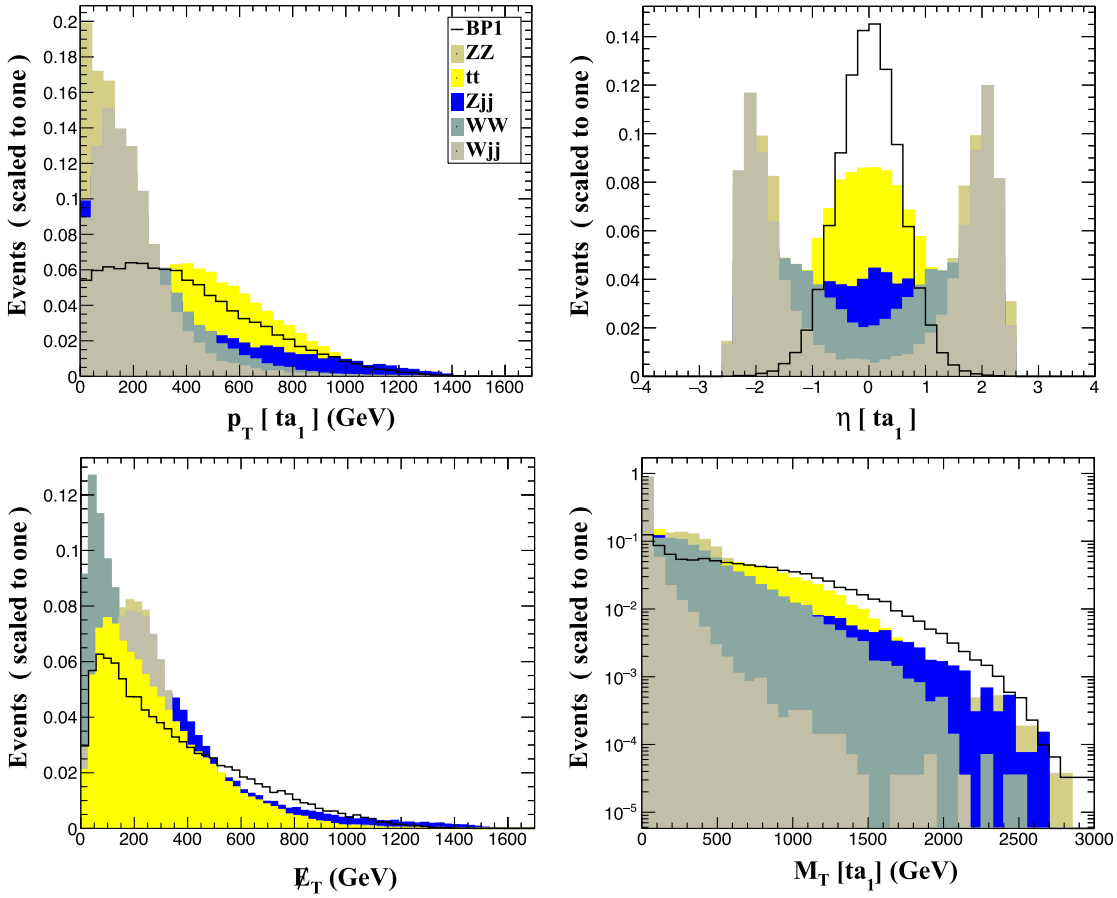

FIG. 10. Normalized kinematic distributions for the final state $\tau^+\nu\tau^-\bar{\nu}$: transverse momentum of the leading tau lepton (ordered in p_T) $p_T[\tau_1]$ (top-left panel), the pseudorapidity of the leading tau lepton $\eta\,[\tau_1]$ (top-right panel), the transverse energy E_T (lower-left panel), and the transverse mass $M_T\ [\tau_1]$ (lower-right panel) at $\sqrt{s} = 3$ TeV muon collider.

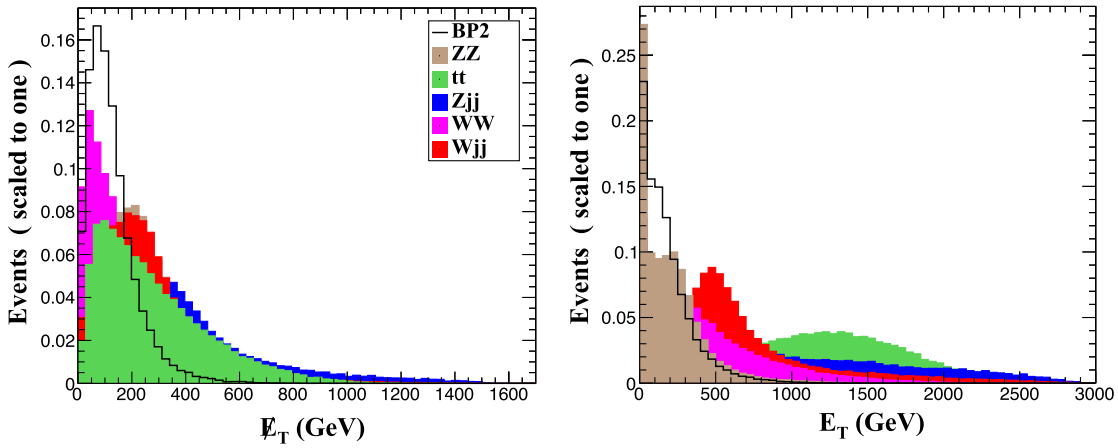

FIG. 11. Normalized kinematic distributions of the signal and backgrounds for the VBF production: the missing transverse energy $\not{E}_T$ (left panel) and the transverse energy E_T (right panel) at $\sqrt{s} = 3$ TeV muon collider.

$$I(P) = \frac{1}{p_T^P} \Sigma p_{T_i} < 0.01.$$

Figure 10 presents the distributions for the transverse momentum of the leading tau lepton $p_T[\tau_1]$ (ordered by p_T), the pseudorapidity of the leading tau $\eta[\tau_1]$, transverse mass $M_T[\tau_1]$, and the transverse energy for the signal benchmark point $BP1$ and various SM backgrounds at the 3 GeV muon collider. In order to increase the significance of the signal, we have established a cut-flow (see Table V) based on the behavior of the kinematic distributions, as presented in Table VII. We start by limiting the number of b-quark N(b) ≤ 1, which is vital in discriminating the signal from the background. Under this cut the $t\bar{t}$ background survived only 47% of events without putting any impact on the signal events. The first selection cut imposed is $P_T[\tau_1] > 60$ GeV and $-0.5 < \eta[\tau_1] < 0.5$ going together for the detection of the tau leptons; under this cut significantly reduces a substantial portion of the background, particularly eliminating the majority of Wjj, ZZ, WW, and Zjj events. The next cut is the missing energy requirement $\not{E}_T > 500$ GeV, which removes about 53% of the tt, 72% of the Zjj, 64% of WW events, while the survival rate for the signal is more than 43%. The lower-right panel (last selection cut) in Fig. 10 indicates a transverse momentum $M_T[\tau_1] > 600$ GeV cut would be useful, which constitutes the "cut 3." It removes about 94% of Wjj while 97% of the signal survives. For the VBF

TABLE V. A set of cuts used in the signal-background analysis of $\mu^+\mu^- \to H^+H^- \to \tau_h^+\nu\tau_h^-\nu$ at $\sqrt{s} = 3$ TeV.

Cuts	Definition
Trigger	$N(b) \leq 1$
Cut 1	$P_T[\tau_1] > 60$ GeV and $-0.5 < \eta[\tau_1] < 0.5$
Cut 2	$\not{E}_T > 600$ GeV
Cut 3	$M_T[\tau_1] > 600$ GeV

TABLE VI. A set of cuts used in the signal-background analysis of VBF at $\sqrt{s} = 3$ TeV.

Cuts	Definition
Trigger	$N(b) \leq 1$
Cut 1	$\not{E}_T < 180$ GeV
Cut 2	$\not{E}_T < 300$ GeV

TABLE VII. The cut flow of the cross sections (in fb) for the signal and SM backgrounds at $\sqrt{s} = 3$ TeV muon collider with our typical BP1.

	Signal	Backgrounds				
Cuts	BP1	$t\bar{t}$	WW	ZZ	Wjj	$Z/\gamma jj$
Basic cut	2.98	0.2	1.54	0.014	7.04	0.74
Tagger	2.97	0.09	1.53	0.014	6.39	0.68
Cut 1	0.72	0.04	0.052	0.0001	0.048	0.02
Cut 2	0.31	0.009	0.018	9.10^{-5}	0.021	0.006
Cut 3	0.30	0.008	0.017	9.10^{-5}	0.0014	0.005
Total efficiencies	10.4%	4%	1.1%	0.6%	2.10^{-2}%	0.6%

TABLE VIII. The cut flow of the cross sections (in fb) for the VBF signal and SM backgrounds at $\sqrt{s} = 3$ TeV muon collider with our typical BP2.

	Signal	Backgrounds				
Cuts	BP2	$t\bar{t}$	WW	ZZ	Wjj	$Z/\gamma jj$
Basic cut	2.35	0.2	1.54	0.014	7.01	0.743
Tagger	2.34	0.09	1.53	0.014	6.38	0.68
Cut 1	1.85	0.03	0.94	0.005	2.44	0.2
Cut 2	1.66	0.0009	0.52	0.005	0.23	0.024
Total efficiencies	70%	0.45%	33%	35%	3.2%	3.2%

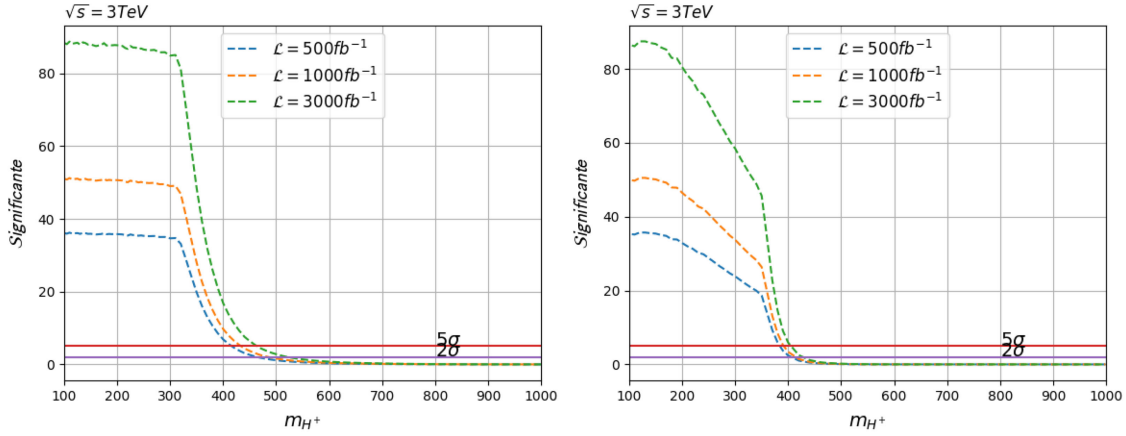

FIG. 12. The significance obtained for the process $\mu^+\mu^- \to H^+H^- \to \tau^+\nu\tau^-\nu$ (left panel) and VBF production (right panel) versus the charged-Higgs mass at 3 TeV muon collider with integrated luminosities of 500, 1000, and 3000 fb^{-1}. The 2σ and 5σ significance levels are also indicated.

production, the cuts are totally different (see Table VI), as shown in Fig. 11. For the achieved signal and background separation, as presented in Table VIII for the signal and background, we impose number of b quark N(b) ≤ 1. The first selection cut applied is $E_T < 180$ GeV. Following, by imposing $E_T < 300$ GeV, under this cut the $t\bar{t}$ and Wjj background events are totally killed.

The left panel in Fig. 12 presents the significance (S) as a function of charged-Higgs boson mass m_{H^+} of the process $\mu^+\mu^- \to H^+H^-$ at $\sqrt{s} = 3$ TeV TeV for various integrated luminosities $\mathcal{L} = 500$, 1000, and 3000 fb^{-1}, wherein the red solid line denotes the 5σ discovery and the purple solid line denotes the 2σ exclusion. With the mere integrated luminosities of 500, 1000, and 3000 fb^{-1}, the outlook for significance seems highly promising. The prospects for significance appear highly promising. the region $m_{H^+} \in [100\ \text{GeV}, 450\ \text{GeV}]$ can be discovered. In the right panel, we show the significance for the VBF channels at e^+e^- machines. Furthermore, the discovery 5σ level achieved at various integrated luminosities $\mathcal{L} = 500$, 1000, and 3000 fb^{-1} in the range masses $m_{H^+} \in [100\ \text{GeV}, 405\ \text{GeV}]$. In summary, we have demonstrated the feasibility of achieving highly favorable signal identification over the standard model backgrounds in the context of charged Higgs production, considering both direct $\mu^+\mu^-$ and the vector boson fusion (VBF) channels.

C. $\mu^+\mu^- \to H^\pm W^\mp$

The most important production channel for the charged Higgs is the associated production with a W boson, which merits particular attention. The Feynman diagrams for the process are modeled in four separate subprocesses, as illustrated in Fig. 2, each of which contributes to the $H^\pm W^\pm$ production cross section. We explore the following final state:

$$\mu^+\mu^- \to H^\pm W^\mp \to \tau^+\nu\tau^-\nu.$$

The corresponding SM backgrounds that can mimic our final state are listed above.

At parton level, the events of the signal and backgrounds are required to pass through the basic cuts as follows:

$$p_T^j > 20, \qquad |\eta^j| < 2.5.$$

We show in Fig. 13 the kinematic distributions of the signal and backgrounds for the missing momentum E_T (upper-left panel) and the transverse energy E_T (upper-right panel) at 3 TeV muon collider. To enhance the signal significance, we have implemented a cut-flow strategy guided by the kinematic distributions, outlined in Table X. The initial step involves restricting the count of b quarks, ensuring $N(b) \leq 1$. This constraint proves crucial in differentiating the signal from the background. With this cut, the $t\bar{t}$ background retains only 47% of events, while minimally affecting the signal events. As shown in the upper-left panel, E_T plays a censorious role in separating the signal from the background. So, we apply $E_T < 75$ GeV. Under this cut alone the surviving rate of the dominant backgrounds Wjj is about 12% and other backgrounds have already become very small, while the signal survival rate is about 67%. We investigate one of the most efficient cuts $E_T < 250$ GeV, which keeps about 95% of the signal events and removes more than 92% of $t\bar{t}$, Zjj, WW, and Wjj background events. The selection cuts imposing are listed in Table IX.

Figure 14 illustrates the 5σ and 2σ limit capability in the significance-m_{H^+} plane at $\sqrt{s} = 3$ TeV for various integrated luminosities. As shown, the significance is presented as a function of m_{H^+} for integrated luminosities of $\mathcal{L} = 500$, 1000, and 3000 fb^{-1}. We observe that a significance of 5σ can be achieved when the integrated luminosity 3000 fb^{-1}. The range of m_{H^+} between around 100 and

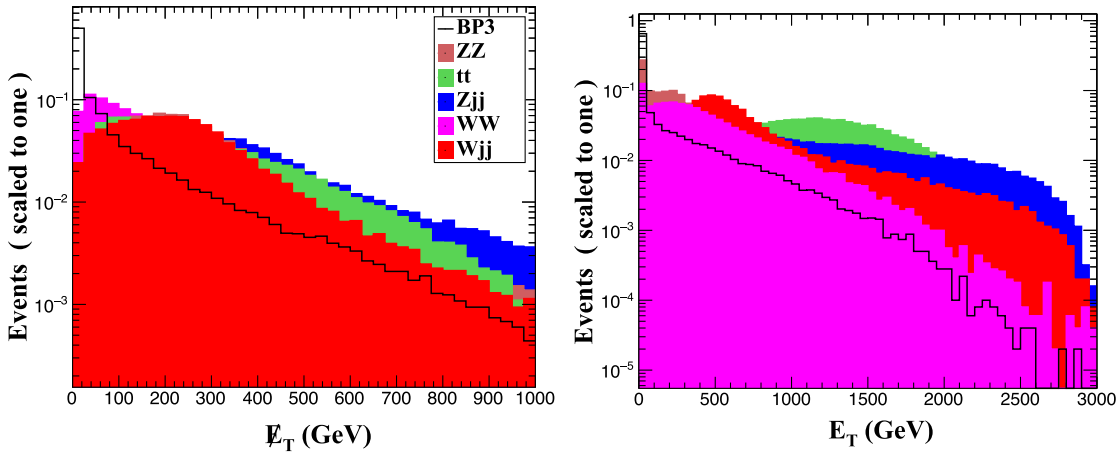

FIG. 13. Normalized kinematic distributions of the signal and backgrounds: the missing transverse energy $\not{E}_T$ (left panel) and the transverse energy E_T (right panel) at $\sqrt{s} = 3$ TeV muon collider.

250 GeV is the most preferred region to discover the charged Higgs boson at $\sqrt{s} = 3$ TeV muon collider. However, the 2σ level achieved within integrated luminosities 500 and 1000 fb^{-1}. The integrated luminosities of $\mathcal{L} = 500$ and 1000 fb^{-1} are significantly not very promising. We find that under these integrated luminosities the significance becomes small, and the 5σ level cannot be achieved under the available charged Higgs mass. In conclusion, it can be inferred that the values of integrated luminosities higher than 3000 fb^{-1} have a vital impact on achieving the 5σ and 2σ significance. This also holds true for the quest to discover the charged Higgs boson $H^{\pm}$ through the process $\mu^+\mu^- \to H^{\pm}W^{\mp}$.

TABLE IX. A set of cuts used in the signal-background analysis for $\mu^+\mu^- \to H^{\pm}W^{\mp} \to \tau^+\nu_\tau\tau^-\nu_\tau$ at $\sqrt{s} = 3$ TeV.

Cuts	Definition
Trigger	$N(b) < 1$
Cut 1	$E_T < 75$ GeV
Cut 2	$E_T < 250$ GeV

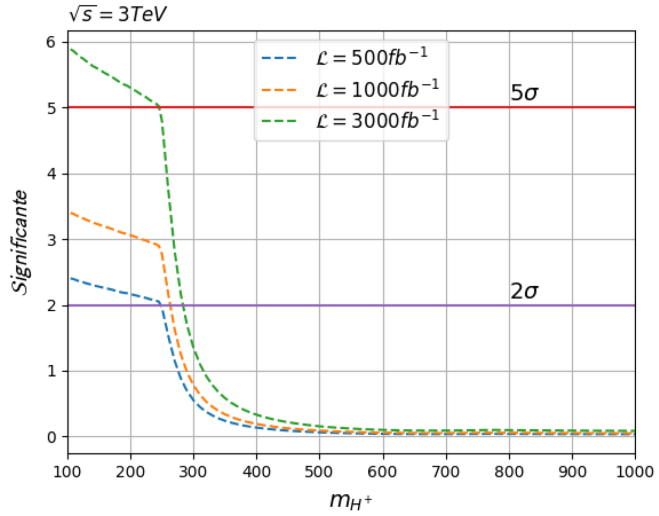

FIG. 14. The significance obtained for the process $\mu^+\mu^- \to H^{\pm}W^{\mp} \to \tau^+\nu_\tau\tau^-\nu_\tau$ versus the charged-Higgs mass at 3 TeV muon collider with integrated luminosities of 500, 1000, and 3000 fb^{-1} with our benchmark point BP3. The 2σ and 5σ significance levels are also indicated.

VI. CONCLUSIONS

We have investigated the charged Higgs production at the upcoming muon collider in the framework of 2HDM. We have studied both $\mu^+\mu^- \to H^+H^-$ and $\mu^+\mu^- \to W^{\pm}H^{\mp}$ and given the analytical amplitudes for various Yukawa textures of the 2HDM. The study was done taking into account theoretical constraints as well as experimental ones such as LHC Higgs searches as well as several B physics measurements. We demonstrated that one may obtain significant improvement for $\mu^+\mu^- \to H^+H^-$ compared to what we can obtain for $e^+e^- \to H^+H^-$, which is achieved by large $\tan\beta$ amplification in the case of type X. Such large $\tan\beta$ in the 2HDM type X survive all kinds of

TABLE X. The cut flow of the cross sections (in fb) for the signal and SM backgrounds at $\sqrt{s} = 3$ TeV muon collider with our typical BP3.

	Signal	Backgrounds				
Cuts	BP3	$t\bar{t}$	WW	ZZ	Wjj	$Z/\gamma jj$
Basic cut	0.064	0.2	1.54	0.014	7.04	0.74
Tagger	0.064	0.09	1.53	0.014	6.39	0.68
Cut 1	0.043	0.01	0.45	0.0014	0.77	0.073
Cut 2	0.0416	0.0004	0.24	0.0014	0.068	0.002
Total efficiencies	64%	0.2%	15%	10%	9.6%	0.27%

experimental or theoretical constraints. The charged-Higgs boson can be probed through $\mu^+\mu^- \to H^+H^-$ only for $m_{H^\pm} < \sqrt{s}/2$. On the other side, $\mu^+\mu^- \to W^\pm H^\mp$ can be used to probe the charged Higgs boson in the region $\sqrt{s}/2 \leq m_{H^\pm} \leq \sqrt{s} - m_W$, for which the charged-Higgs pair production is not accessible. We have shown that in this region one can still have a significant cross section for $\mu^+\mu^- \to W^\pm H^\mp$.

In the case of light charged Higgs boson mass, a significant enhancement in the production cross section VBF $e^+e^- \to \nu_e\bar{\nu}_e H^+H^-$ may be obtained which makes this $2 \to 4$ process compete with the other $2 \to 2$. All the results presented for type X are also valid for type II if we take into account constraints from B physics that request that the charged Higgs should be heavier that 680 GeV and well as $\tan\beta \leq 12$ as suggested by LHC Higgs data. However, once the charged Higgs boson is heavier than 680 GeV in type II, the sensitivity is completely lost. We have also performed a signal-background analysis and obtained the discovery 5σ region and the exclusion region 2σ at 3 TeV muon collider both for $\mu^+\mu^- \to H^+H^-$, $\mu^+\mu^- \to W^\pm H^\mp$ as well as VBF.

ACKNOWLEDGMENTS

This work is supported by the Moroccan Ministry of Higher Education and Scientific Research MESRSFC and CNRST: Project No. PPR/2015/6. K. C. is supported in part by the National Science and Technology Council of Taiwan under the Grant No. MoST 110-2112-M-007-017-MY3.

[1] G. Aad *et al.* (ATLAS Collaboration), Observation of a new particle in the search for the Standard Model Higgs boson with the ATLAS detector at the LHC, Phys. Lett. B **716**, 1 (2012).
[2] S. Chatrchyan *et al.* (CMS Collaboration), Observation of a new boson at a mass of 125 GeV with the CMS experiment at the LHC, Phys. Lett. B **716**, 30 (2012).
[3] G. Aad *et al.* (ATLAS Collaboration), A detailed map of Higgs boson interactions by the ATLAS experiment ten years after the discovery, Nature (London) **607**, 52 (2022).
[4] A. Tumasyan *et al.* (CMS Collaboration), A portrait of the Higgs boson by the CMS experiment ten years after the discovery, Nature (London) **607**, 60 (2022).
[5] L. Rossi, HL-LHC Preliminary Design Report: Deliverable: D1.5; CERN: Geneva, Switzerland, 2014.
[6] B. Ait-Ouazghour and M. Chabab, The Higgs potential in 2HDM extended with a real triplet scalar: A roadmap, Int. J. Mod. Phys. A **36**, 2150131 (2021).
[7] B. Grzadkowski, P. Osland, and J. Wudka, Pragmatic extensions of the standard model, Acta Phys. Pol. B **42**, 2245 (2011).
[8] C. N. Karahan and B. Korutlu, Effects of a real singlet scalar on Veltman condition, Phys. Lett. B **732**, 320 (2014).
[9] N. Darvishi and M. Krawczyk, Implication of quadratic divergences cancellation in the two Higgs doublet model, Nucl. Phys. **B926**, 167 (2018).
[10] B. A. Ouazghour, A. Arhrib, R. Benbrik, M. Chabab, and L. Rahili, Theory and phenomenology of a two-Higgs-doublet type-II seesaw model at the LHC run 2, Phys. Rev. D **100**, 035031 (2019).
[11] G. C. Branco, P. M. Ferreira, L. Lavoura, M. N. Rebelo, M. Sher, and J. P. Silva, Theory and phenomenology of two-Higgs-doublet models, Phys. Rep. **516**, 1 (2012).
[12] A. G. Akeroyd *et al.*, Prospects for charged Higgs searches at the LHC, Eur. Phys. J. C **77**, 276 (2017).
[13] S. Komamiya, Searching for charged Higgs bosons at ~(1/2–1-TeV) e^+e^- colliders, Phys. Rev. D **38**, 2158 (1988).
[14] A. Arhrib and G. Moultaka, Radiative corrections to $e^+e^- \to H^+H^-$: THDM versus MSSM, Nucl. Phys. **B558**, 3 (1999).
[15] J. Guasch, W. Hollik, and A. Kraft, Radiative corrections to pair production of charged Higgs bosons in e^+e^- collisions, Nucl. Phys. **B596**, 66 (2001).
[16] A. Arhrib, M. Capdequi Peyranere, W. Hollik, and G. Moultaka, Associated H^-W^+ production in high-energy e^+e^- collisions, Nucl. Phys. **B581**, 34 (2000).
[17] S. Kanemura, Possible enhancement of the $e^+e^- \to H^\pm W^\pm$ cross-section in the two Higgs doublet model, Eur. Phys. J. C **17**, 473 (2000).
[18] S. Heinemeyer and C. Schappacher, Charged Higgs boson production at e^+e^- colliders in the complex MSSM: A full one-loop analysis, Eur. Phys. J. C **76**, 535 (2016).
[19] O. Brein and T. Hahn, On MSSM charged Higgs boson production in association with an electroweak W boson at electron positron colliders, Eur. Phys. J. C **52**, 397 (2007).
[20] H. E. Logan and S.-f. Su, Variation of the cross section for $e^+e^- \to W^+H^-$ in the minimal supersymmetric standard model, Phys. Rev. D **67**, 017703 (2003).
[21] F. Kling, S. Su, and W. Su, 2HDM neutral scalars under the LHC, J. High Energy Phys. 06 (2020) 163.
[22] T. Abe *et al.*, Linear collider physics resource book for Snowmass 2001, arXiv:hep-ex/0106055.
[23] T. Abe *et al.* (Linear Collider American Working Group Collaboration), Linear collider physics resource book for Snowmass 2001—Part 2: Higgs and supersymmetry studies, in APS/DPF/DPB Summer Study on the Future of Particle Physics (2001), arXiv:hep-ex/0106056.
[24] T. Abe *et al.* (Linear Collider American Working Group Collaboration), Linear collider physics resource book for Snowmass 2001—Part 3: Studies of exotic and standard model physics, arXiv:hep-ex/0106057.
[25] F. An *et al.*, Precision Higgs physics at the CEPC, Chin. Phys. C **43**, 043002 (2019).

[26] E. Accomando *et al.* (CLIC Physics Working Group), Physics at the CLIC multi-TeV linear collider, in *11th International Conference on Hadron Spectroscopy*, CERN Yellow Reports: Monographs Vol. 6 (2004), arXiv:hep-ph/0412251.

[27] A multi-TeV linear collider based on CLIC tchnology: CLIC conceptual design report, 2012, https://doi.org/10.5170/CERN-2012-007.

[28] A. Abada *et al.* (FCC Collaboration), FCC-ee: The lepton collider: Future circular collider conceptual design report Volume 2, Eur. Phys. J. Special Topics **228**, 261 (2019).

[29] M. Bicer *et al.* (TLEP Design Study Working Group), First look at the physics case of TLEP, J. High Energy Phys. 01 (2014) 164.

[30] K. Fujii *et al.* (LCC Physics Working Group), Tests of the standard model at the international linear collider, arXiv:1908.11299.

[31] A. Arbey *et al.*, Physics at the e^+e^- linear collider, Eur. Phys. J. C **75**, 371 (2015).

[32] S. Bhattacharya, S. Jahedi, and J. Wudka, Optimal determination of new physics couplings: A comparative study, J. High Energy Phys. 12 (2023) 026.

[33] J. P. Delahaye, M. Diemoz, K. Long, B. Mansoulié, N. Pastrone, L. Rivkin, D. Schulte, A. Skrinsky, and A. Wulzer, Muon colliders, arXiv:1901.06150.

[34] T. Han, Y. Ma, and K. Xie, High energy leptonic collisions and electroweak parton distribution functions, Phys. Rev. D **103**, L031301 (2021).

[35] K. Long, D. Lucchesi, M. Palmer, N. Pastrone, D. Schulte, and V. Shiltsev, Muon colliders: Opening new horizons for particle physics, Nat. Phys. **17**, 289 (2021).

[36] T. Han, Z. Liu, L.-T. Wang, and X. Wang, WIMPs at high energy muon colliders, Phys. Rev. D **103**, 075004 (2021).

[37] A. Costantini, F. De Lillo, F. Maltoni, L. Mantani, O. Mattelaer, R. Ruiz, and X. Zhao, Vector boson fusion at multi-TeV muon colliders, J. High Energy Phys. 09 (2020) 080.

[38] T. Han, S. Li, S. Su, W. Su, and Y. Wu, Heavy Higgs bosons in 2HDM at a muon collider, Phys. Rev. D **104**, 055029 (2021).

[39] N. Vignaroli, Charged resonances and MDM bound states at a multi-TeV muon collider, J. High Energy Phys. 10 (2023) 121.

[40] R. Capdevilla, D. Curtin, Y. Kahn, and G. Krnjaic, A no-lose theorem for discovering the new physics of $(g-2)_\mu$ at muon colliders, Phys. Rev. D **105**, 015028 (2022).

[41] W. Liu and K.-P. Xie, Probing electroweak phase transition with multi-TeV muon colliders and gravitational waves, J. High Energy Phys. 04 (2021) 015.

[42] G.-y. Huang, F. S. Queiroz, and W. Rodejohann, Gauged $L_\mu - L_\tau$ at a muon collider, Phys. Rev. D **103**, 095005 (2021).

[43] W. Yin and M. Yamaguchi, Muon $g-2$ at multi-TeV muon collider, Phys. Rev. D **106**, 033007 (2022).

[44] D. Buttazzo and P. Paradisi, Probing the muon $g-2$ anomaly at a muon collider, Phys. Rev. D **104**, 075021 (2021).

[45] R. Capdevilla, D. Curtin, Y. Kahn, and G. Krnjaic, A guaranteed discovery at future muon colliders, Phys. Rev. D **103**, 075028 (2021).

[46] T. Han, D. Liu, I. Low, and X. Wang, Electroweak couplings of the Higgs boson at a multi-TeV muon collider, Phys. Rev. D **103**, 013002 (2021).

[47] A. G. Akeroyd, A. Arhrib, and C. Dove, Charged and pseudoscalar Higgs production at a muon collider, Phys. Rev. D **61**, 071702 (2000).

[48] M. Hashemi, Charged Higgs observability through associated production with W at a muon collider, Eur. Phys. J. C **72**, 2207 (2012).

[49] A. G. Akeroyd and S. Baek, Single charged Higgs production as a probe of *CP* violation at a muon collider, Phys. Lett. B **500**, 142 (2001),

[50] T. D. Lee, A theory of spontaneous T violation, Phys. Rev. D **8**, 1226 (1973).

[51] E. A. Paschos, Diagonal neutral currents, Phys. Rev. D **15**, 1966 (1977).

[52] S. L. Glashow and S. Weinberg, Natural conservation laws for neutral currents, Phys. Rev. D **15**, 1958 (1977).

[53] S. Kanemura, T. Kubota, and E. Takasugi, Lee-Quigg-Thacker bounds for Higgs boson masses in a two doublet model, Phys. Lett. B **313**, 155 (1993),

[54] A. G. Akeroyd, A. Arhrib, and E.-M. Naimi, Note on tree level unitarity in the general two Higgs doublet model, Phys. Lett. B **490**, 119 (2000),

[55] A. Arhrib, Unitarity constraints on scalar parameters of the standard and two Higgs doublets model, in *Workshop on Noncommutative Geometry, Superstrings and Particle Physics* (2000), arXiv:hep-ph/0012353.

[56] A. Barroso, P. M. Ferreira, I. P. Ivanov, and R. Santos, Metastability bounds on the two Higgs doublet model, J. High Energy Phys. 06 (2013) 045.

[57] N. G. Deshpande and E. Ma, Pattern of symmetry breaking with two Higgs doublets, Phys. Rev. D **18**, 2574 (1978).

[58] M. E. Peskin and T. Takeuchi, Estimation of oblique electroweak corrections, Phys. Rev. D **46**, 381 (1992).

[59] C.-T. Lu, L. Wu, Y. Wu, and B. Zhu, Electroweak precision fit and new physics in light of the W boson mass, Phys. Rev. D **106**, 035034 (2022).

[60] D. Eriksson, J. Rathsman, and O. Stal, 2HDMC: Two-Higgs-doublet model calculator physics and manual, Comput. Phys. Commun. **181**, 189 (2010).

[61] P. Bechtle, D. Dercks, S. Heinemeyer, T. Klingl, T. Stefaniak, G. Weiglein, and J. Wittbrodt, HiggsBounds-5: Testing Higgs sectors in the LHC 13 TeV era, Eur. Phys. J. C **80**, 1211 (2020).

[62] P. Bechtle, S. Heinemeyer, O. Stal, T. Stefaniak, and G. Weiglein, Applying exclusion likelihoods from LHC searches to extended Higgs sectors, Eur. Phys. J. C **75**, 421 (2015).

[63] P. Bechtle, S. Heinemeyer, T. Klingl, T. Stefaniak, G. Weiglein, and J. Wittbrodt, HiggsSignals-2: Probing new physics with precision Higgs measurements in the LHC 13 TeV era, Eur. Phys. J. C **81**, 145 (2021).

[64] A. M. Sirunyan *et al.* (CMS Collaboration), Search for a new scalar resonance decaying to a pair of Z bosons in proton-proton collisions at $\sqrt{s} = 13$ TeV, J. High Energy Phys. 06 (2018) 127; J. High Energy Phys. 03 (2019) 128(E).

[65] A. M. Sirunyan *et al.* (CMS Collaboration), Search for a heavy pseudoscalar boson decaying to a Z and a Higgs boson at $\sqrt{s} = 13$ TeV, Eur. Phys. J. C **79**, 564 (2019).

[66] G. Aad *et al.* (ATLAS Collaboration), Search for heavy Higgs bosons decaying into two tau leptons with the ATLAS detector using pp collisions at $\sqrt{s} = 13$ TeV, Phys. Rev. Lett. **125**, 051801 (2020).

[67] M. Aaboud *et al.* (ATLAS Collaboration), Combination of searches for heavy resonances decaying into bosonic and leptonic final states using 36 fb^{-1} of proton-proton collision data at $\sqrt{s} = 13$ TeV with the ATLAS detector, Phys. Rev. D **98**, 052008 (2018).

[68] M. Aaboud *et al.* (ATLAS Collaboration), Search for a heavy Higgs boson decaying into a Z boson and another heavy Higgs boson in the $\ell\ell bb$ final state in pp collisions at $\sqrt{s} = 13$ TeV with the ATLAS detector, Phys. Lett. B **783**, 392 (2018).

[69] G. Aad *et al.* (ATLAS Collaboration), Search for heavy resonances decaying into a Z or W boson and a Higgs boson in final states with leptons and b-jets in 139 fb^{-1} of pp collisions at $\sqrt{s} = 13$ TeV with the ATLAS detector, arXiv:2207.00230.

[70] CMS Collaboration, Search for the standard model Higgs boson decaying to tau pairs, Report No. CMS-PAS-HIG-12-043, 2012.

[71] G. Aad *et al.* (ATLAS Collaboration), Search for a CP-odd Higgs boson decaying to Zh in pp collisions at $\sqrt{s} = 8$ TeV with the ATLAS detector, Phys. Lett. B **744**, 163 (2015).

[72] M. Aaboud *et al.* (ATLAS Collaboration), Search for charged Higgs bosons decaying via $H^\pm \to \tau^\pm \nu_\tau$ in the $\tau +$ jets and $\tau +$ lepton final states with 36 fb^{-1} of pp collision data recorded at $\sqrt{s} = 13$ TeV with the ATLAS experiment, J. High Energy Phys. 09 (2018) 139.

[73] V. Khachatryan *et al.* (CMS Collaboration), Search for a charged Higgs boson in pp collisions at $\sqrt{s} = 8$ TeV, J. High Energy Phys. 11 (2015) 018.

[74] CMS Collaboration, Search for additional neutral Higgs bosons decaying to a pair of tau leptons in pp collisions at $\sqrt{s} = 7$ and 8 TeV, CERN, Geneva Switzerland, Report No. CMS-PAS-HIG-14-029, 2014.

[75] A. M. Sirunyan *et al.* (CMS Collaboration), Search for additional neutral MSSM Higgs bosons in the $\tau\tau$ final state in proton-proton collisions at $\sqrt{s} = 13$ TeV, J. High Energy Phys. 09 (2018) 007.

[76] V. Khachatryan *et al.* (CMS Collaboration), Search for neutral resonances decaying into a Z boson and a pair of b jets or τ leptons, Phys. Lett. B **759**, 369 (2016).

[77] ALEPH, DELPHI, L3, OPAL, LEP Collaborations, Search for charged Higgs bosons: Combined results using LEP data, Eur. Phys. J. C **73**, 2463 (2013).

[78] M. Aaboud *et al.* (ATLAS Collaboration), Search for Higgs boson pair production in the $\gamma\gamma b\bar{b}$ final state with 13 TeV pp collision data collected by the ATLAS experiment, J. High Energy Phys. 11 (2018) 040.

[79] ATLAS Collaboration, Search for charged Higgs bosons decaying into a top-quark and a bottom-quark at $\sqrt{s} =$ 13 TeV with the ATLAS detector, CERN, Geneva, Report No. ATLAS-CONF-2020-039, 2020.

[80] G. Aad *et al.* (ATLAS Collaboration), Search for neutral Higgs bosons of the minimal supersymmetric standard model in pp collisions at $\sqrt{s} = 8$ TeV with the ATLAS detector, J. High Energy Phys. 11 (2014) 056.

[81] M. Aaboud *et al.* (ATLAS Collaboration), Search for new phenomena in high-mass diphoton final states using 37 fb^{-1} of proton-proton collisions collected at $\sqrt{s} = 13$ TeV with the ATLAS detector, Phys. Lett. B **775**, 105 (2017).

[82] M. Aaboud *et al.* (ATLAS Collaboration), Search for pair production of Higgs bosons in the $b\bar{b}b\bar{b}$ final state using proton-proton collisions at $\sqrt{s} = 13$ TeV with the ATLAS detector, J. High Energy Phys. 01 (2019) 030.

[83] G. Aad *et al.* (ATLAS Collaboration), Combination of searches for Higgs boson pairs in pp collisions at $\sqrt{s} =$ 13 TeV with the ATLAS detector, Phys. Lett. B **800**, 135103 (2020).

[84] A. M. Sirunyan *et al.* (CMS Collaboration), Search for a charged Higgs boson decaying to charm and bottom quarks in proton-proton collisions at $\sqrt{s} = 8$ TeV, J. High Energy Phys. 11 (2018) 115.

[85] A. M. Sirunyan *et al.* (CMS Collaboration), Search for heavy Higgs bosons decaying to a top quark pair in proton-proton collisions at $\sqrt{s} = 13$ TeV, J. High Energy Phys. 04 (2020) 171; J. High Energy Phys. 03 (2022) 187(E).

[86] F. Mahmoudi, Superiso v2.3: A program for calculating flavor physics observables in supersymmetry, Comput. Phys. Commun. **180**, 1579 (2009).

[87] T. Hahn, Generating Feynman diagrams and amplitudes with FeynArts 3, Comput. Phys. Commun. **140**, 418 (2001).

[88] T. Hahn and M. Perez-Victoria, Automatized one loop calculations in four-dimensions and D-dimensions, Comput. Phys. Commun. **118**, 153 (1999).

[89] T. Hahn and C. Schappacher, The implementation of the minimal supersymmetric standard model in FeynArts and FormCalc, Comput. Phys. Commun. **143**, 54 (2002).

[90] J. Kublbeck, M. Bohm, and A. Denner, FeynArts: Computer algebraic generation of Feynman graphs and amplitudes, Comput. Phys. Commun. **60**, 165 (1990).

[91] J. F. Gunion and H. E. Haber, The CP conserving two Higgs doublet model: The approach to the decoupling limit, Phys. Rev. D **67**, 075019 (2003).

[92] J. Haller, A. Hoecker, R. Kogler, K. Mönig, T. Peiffer, and J. Stelzer, Update of the global electroweak fit and constraints on two-Higgs-doublet models, Eur. Phys. J. C **78**, 675 (2018).

[93] Y. Amhis *et al.* (HFLAV Collaboration), Averages of b-hadron, c-hadron, and τ-lepton properties as of summer 2016, Eur. Phys. J. C **77**, 895 (2017).

[94] T. Hermann, M. Misiak, and M. Steinhauser, $\bar{B} \to X_s\gamma$ in the two Higgs doublet model up to next-to-next-to-leading order in QCD, J. High Energy Phys. 11 (2012) 036.

[95] M. Misiak and M. Steinhauser, Weak radiative decays of the B meson and bounds on $M_{H^\pm}$ in the two-Higgs-doublet model, Eur. Phys. J. C **77**, 201 (2017).

[96] M. Misiak, A. Rehman, and M. Steinhauser, Towards $\bar{B} \to X_s\gamma$ at the NNLO in QCD without interpolation in m_c, J. High Energy Phys. 06 (2020) 175.

[97] J. Alwall, R. Frederix, S. Frixione, V. Hirschi, F. Maltoni, O. Mattelaer, H. S. Shao, T. Stelzer, P. Torrielli, and M. Zaro, The automated computation of tree-level and next-to-leading order differential cross sections, and their matching to parton shower simulations, J. High Energy Phys. 07 (2014) 079.

[98] T. Sjostrand, S. Mrenna, and P. Z. Skands, A brief introduction to PYTHIA 8.1, Comput. Phys. Commun. **178**, 852 (2008).

[99] J. de Favereau, C. Delaere, P. Demin, A. Giammanco, V. Lemaître, A. Mertens, and M. Selvaggi (DELPHES 3 Collaboration), DELPHES 3, A modular framework for fast simulation of a generic collider experiment, J. High Energy Phys. 02 (2014) 057.

[100] M. Cacciari, G. P. Salam, and G. Soyez, The anti-k_t jet clustering algorithm, J. High Energy Phys. 04 (2008) 063.